Journal of The Electrochemical Society

Multidimensional Cyclic Voltammetry Simulations of Pseudocapacitive Electrodes with a Conducting Nanorod Scaffold

To cite this article: Bing-Ang Mei *et al* 2017 *J. Electrochem. Soc.* **164** A3237

Multidimensional Cyclic Voltammetry Simulations of Pseudocapacitive Electrodes with a Conducting Nanorod Scaffold

Bing-Ang Mei, Bin Li, Jie Lin, and Laurent Pilon*,z

Henry Samueli School of Engineering and Applied Science, Mechanical and Aerospace Engineering Department, University of California, Los Angeles, Los Angeles, California 90095, USA

This paper aims to understand the effect of nanoarchitecture on the performance of pseudocapacitive electrodes consisting of conducting scaffold coated with pseudocapacitive material. To do so, two-dimensional numerical simulations of ordered conducting nanorods coated with a thin film of pseudocapacitive material were performed. The simulations reproduced three-electrode cyclic voltammetry measurements based on a continuum model derived from first principles. Two empirical approaches commonly used experimentally to characterize the contributions of surface-controlled and diffusion-controlled charge storage mechanisms to the total current density with respect to scan rate were theoretically validated for the first time. Moreover, the areal capacitive capacitance, attributed to EDL formation, remained constant and independent of electrode dimensions, at low scan rates. However, at high scan rates, it decreased with decreasing conducting nanorod radius and increasing pseudocapacitive layer thickness due to resistive losses. By contrast, the gravimetric faradaic capacitance, due to reversible faradaic reactions, decreased continuously with increasing scan rate and pseudocapacitive layer thickness but was independent of conducting nanorod radius. Note that the total gravimetric capacitance predicted numerically featured values comparable to experimental measurements. Finally, an optimum pseudocapacitive layer thickness that maximizes total areal capacitance was identified as a function of scan rate and confirmed by scaling analysis.
 [DOI: 10.1149/2.1241713jes]

Manuscript submitted August 28, 2017; revised manuscript received October 9, 2017. Published October 27, 2017.

Electrochemical capacitors (ECs) have attracted significant attention in recent years due to their promises as electrical energy storage devices for high power applications.[1,2] They can be classified as either electric double layer capacitors (EDLCs) or pseudocapacitors depending on the charge storage mechanism. EDLCs store energy physically in the electric double layers (EDL) forming at the electrode/electrolyte interfaces.[1,2] They feature fast charging and discharging rates and thus large power density. They also have long cycle life thanks to highly reversible EDL formation. On the other hand, pseudocapacitors store energy both in the EDL and via reversible oxidation-reduction (redox) reactions occurring at the electrode surface and/or involving ion intercalation into the pseudocapacitive material.[1,3–5] By combining both electrical energy storage mechanisms, pseudocapacitors offer the prospect of achieving high power density as well as high energy density.[1,3–5]

Materials for pseudocapacitors typically consist of transition metal oxides or conductive polymers capable of reacting with ions present in the electrolyte (e.g., Li^+, K^+, and H^+).[6] The most commonly used materials for pseudocapacitive electrodes include $RuO_2 \cdot xH_2O$, MnO_2, Mn_3O_4, Nb_2O_5, NiO, CoO_x, Fe_2O_3, Fe_3O_4, V_2O_5, and MoO_3.[3,6–25] Unfortunately, most oxide materials typically feature low electrical conductivity.[8] This may lead to excessive potential drop across thick electrodes and thus limit their energy and power densities.[6,8] One way to avoid excessive potential drops and to improve the performance of pseudocapacitive electrodes is to use an electrically conducting scaffold (e.g., carbon nanotubes) to support thin domains of pseudocapacitive materials.[3,6–14,16–20]

This paper aims to study the effect of electrode nanoarchitecture on the performance of pseudocapacitive electrodes consisting of a layer of pseudocapacitive material deposited on a conducting scaffold. To do so, time-dependent multi-dimensional simulations of conducting nanorods coated with pseudocapacitive material with different dimensions were performed. The model accurately accounted for potential evolution and ion transport occurring in the electrolyte and for both redox reactions and intercalation of the reaction product in the pseudocapacitive layer. This study aims (i) to provide physical interpretations of three-electrode cyclic voltammetry measurements, (ii) to validate empirical data analysis methods commonly used experimentally, and (iii) to derive design rules for the electrode dimensions.

Background

Experimental studies.—To address the problem of low electrical conductivity of pseudocapacitive oxide materials previously mentioned, various nanocomposite electrodes have been synthesized including (i) MnO_2 layer coated on carbon nanotubes,[9] (ii) MnO_2 nanoparticles deposited on carbon nanotubes[10–13] or on carbon nanofoam,[14] (iii) MnO_x nanoparticles grown on carbon nanotube arrays,[15] (iv) Mn_3O_4 nanorods grown on graphene sheets,[16] (v) slurry of mixed carbon nanotubes and redox active material nanoparticles including MnO_2, Fe_3O_4, and V_2O_5,[17–21] (vi) metal oxide materials including $Co_xNi_{1-x}(OH)_2$, MnO_2, and FeOOH deposited on highly conductive $NiCo_2S_4$ nanotube arrays,[22] and (vii) metal oxide materials $Co_xNi_{1-x}(OH)_2$, $Co_xNi_{1-x}O$, and $(Co_xNi_{1-x})_9S_8$ coated on carbon nanotube arrays,[23] (viii) Fe_2O_3 nanoparticles grown on nitrogen-doped graphene,[24] and (ix) Fe_3O_4 nanoparticles grown on graphene nanoplates.[25]

Moreover, the performance of nanocomposite electrodes has been compared with that of electrodes without conducting scaffold.[9,12,13,16,19,20,26] For example, Li et al.[9] fabricated electrodes consisting of single-walled carbon nanotubes coated by a MnO_2 layer to form MnO_2/C nanotube (NT) arrays. The length of the MnO_2/C NTs was 3 μm, while the outer radius of the carbon nanotubes was 550 nm and the thickness of the MnO_2 coating was 100 nm. The distance between adjacent MnO_2/C NTs was large compared with the diameter of the NTs. The gravimetric capacitance of these C/MnO_2 NT electrodes in 0.5 M aqueous Na_2SO_4 electrolyte was 161 F/g at scan rate 5 mV/s, for example. This was significantly larger than the value of 66 F/g, obtained at the same scan rate, for electrodes consisting of MnO_2 nanotubes without carbon nanotube (CNT) scaffold with the same electrode thickness.[9] Similarly, electrodes consisting of MnO_2/C NTs featured larger energy density than MnO_2 NTs without CNT scaffold for a given power density. In addition, the gravimetric capacitance retention of MnO_2/C NT electrodes was 97% after 5,000 cycles compared with 69% for electrodes consisting of MnO_2 NTs. This confirms the positive effect of adding a conducting scaffold on the performance of pseudocapacitive electrodes.

*Electrochemical Society Member.
zE-mail: pilon@seas.ucla.edu

Furthermore, the effects of the conducting scaffold architecture and mass loading of pseudocapacitive materials were also tested experimentally.[10,11,13,19,27] For example, Lee et al.[11] synthesized films of multiwall carbon nanotubes, 100 – 350 nm in thickness, using layer-by-layer assembly. The MWCNTs were 15 ± 5 nm in diameter uniformly coated with MnO_2 nanocrystals about 10 nm in diameter. Performance of these electrodes were compared with that of electrodes consisting of MnO_2 nanocrystals 20 nm in diameter deposited on carbon nanofoam 170 μm in thickness with average pore diameter 30 – 80 nm in 0.1 M aqueous K_2SO_4 electrolyte.[28] The gravimetric capacitance attributed to MnO_2 nanoparticles was significantly larger for electrodes consisting of MnO_2 nanocrystals coated on MWCNT than those consisting of MnO_2 nanocrystals on carbon nanofoam.[28] This was attributed to (i) higher packing density of MWNT network resulting in smaller potential drop from the current collector to the MnO_2 layer and (ii) thinner electrode leading to faster ion diffusion from bulk electrolyte to the electrode surface inside the porous structure. In addition, the authors varied the mass loading of MnO_2 by changing the dipping time[11] and observed an increase in the volumetric capacitance with increasing mass loading of MnO_2.

Empirical characterization of pseudocapacitive electrodes.—A semi-empirical approach for analyzing cyclic voltammetry (CV) measurements has been used extensively[29–36] to determine whether the charge storage process involves (i) surface-controlled mechanism when the measured current density is proportional to scan rate or (ii) diffusion-controlled mechanism when the measured current density is proportional to the square root of scan rate.[37] This approach assumed linear summation of the two contributions to the measured current density j_T at low scan rates according to,[37]

$$j_T(v, \psi_s) = k_1(\psi_s)v + k_2(\psi_s)v^{1/2} \quad \text{or}$$
$$\frac{j_T(v, \psi_s)}{v^{1/2}} = k_1(\psi_s)v^{1/2} + k_2(\psi_s). \qquad [1]$$

Here, $k_1(\psi_s)$ and $k_2(\psi_s)$ are semi-empirical functions associated respectively with surface-controlled and diffusion-controlled mechanisms. They correspond to the slope and intercept in the plot of $j_T/v^{1/2}$ versus $v^{1/2}$ for a given potential $\psi_s(t)$. The functions $k_1(\psi_s)$ and $k_2(\psi_s)$ are independent of scan rate v but depend on the imposed potential ψ_s.[37]

Another approach commonly used experimentally[29,33,34,38–44] assumed that the total current density obeys a power law with respect to the scan rate v according to[38]

$$j_T(v, \psi_s) = a_0(\psi_s)v^{b(\psi_s)} \qquad [2]$$

where the so-called b-value was expected to vary between 1/2 (diffusion-controlled mechanism) and 1 (surface-controlled mechanism).[38] A b-value of 1 across the potential window is highly desirable to achieve high charging rates.[39] Unfortunately, a dip in the b-value when plotted as a function of $\psi_s(t)$ has often been observed experimentally and attributed to the redox peak from faradaic reactions retrieved from CV curves.[29,33,44] However, recent modeling efforts have clarified the physical phenomena responsible for the dip in the b-value.[39]

Finally, note that the above data analysis methods can be applied to the gravimetric (in A/g) or areal (in A/m^2) current densities, or the total current i_T (in A).

Continuum models for simulating pseudocapacitors.—Various continuum models have been developed to predict the capacitance of two-electrode pseudocapacitive devices.[39,45–55] They investigated the effect of electrode composition,[45,49] solid-state ion diffusion in the electrode,[46] and moving reaction fronts.[50] These models assumed constant double layer capacitance throughout the charging/discharging cycle period and uniform ion concentrations throughout the electrolyte.[45,49,50] However, double layer capacitance varied with imposed potential and ion concentrations vary significantly in space and time.[56] In addition, the presence of EDLs near the electrodes can have a significant effect on the redox reactions in pseudocapacitors.[39,45,49,50,53,57,58] More recently, we have developed continuum models for hybrid devices accounting simultaneously for the temporal evolution of the EDL at the electrode/electrolyte interface as well as redox reactions and intercalations under cyclic voltammetry[39] and galvanostatic cycling.[53]

Moreover, experimental characterization of pseudocapacitive electrodes typically uses a three-electrode configuration with the pseudocapacitive electrode of interest serving as the working electrode along with a counter electrode and a reference electrode.[7,9–11,15,19,20,22,23,26–28,30,31,33,36,59–61] Girard et al.[55] simulated three-electrode experiments for planar pseudocapacitive electrodes supported by a planar current collector. Such one-dimensional simulations qualitatively reproduced experimental measurements and provided qualitative physical interpretation of experimentally measured cyclic voltammograms for dense and porous Nb_2O_5 electrodes in $LiClO_4$/PC electrolyte.[7] The authors identified two regimes in the CV curves namely (i) a faradaic regime, in the lower portion of the potential window, where contribution from redox reactions to the total current dominated and (ii) a capacitive regime, in the higher portion of the potential window, where contribution from EDL formation dominated. The transition between the two regimes was responsible for the dip in the b-value and was due to the formation of a ClO_4^- EDL and the starvation of Li^+ in the electrolyte at the electrode/electrolyte interface. However, to the best of our knowledge, previous continuous simulations considered typically planar geometries[39,45–55] but did not account for realistic porous electrode architectures including those with a conducting scaffold supporting a redox active layer. Thus, they could not provide direct quantitative comparison with experimental data or design rules for the electrode architecture.

This paper aims to study the effect of electrode nanoarchitecture on the performance of pseudocapacitive electrodes. To do so, it presents, for the first time, transient multidimensional simulations of pseudocapacitive electrodes consisting of a layer of pseudocapacitive material (e.g., MnO_2) coated on electrically conducting (e.g., carbon) nanorods under cyclic voltammetry. The physical model accurately accounted for (i) redox reactions, (ii) EDL formation at the electrode/electrolyte interface, (iii) multidimensional ion transport in the electrolyte, and (iv) intercalation in the electrode for various conducting nanorod radii and pseudocapacitive layer thicknesses. In particular, this study aims to provide physical interpretation of CV curves by assessing the contribution to charge storage from EDL formation and faradaic reactions. It also aims to theoretically validate semi-empirical approaches commonly used for analyzing cyclic voltammetry measurements, based on Equations 1 and 2. Finally, it illustrates how the physical models and the associated simulations can be used to identify optimum dimensions of the electrode.

Analysis

Schematic and assumptions.—Figure 1a shows the schematic of a pseudocapacitive electrode consisting of a planar current collector of thickness L_s supporting an array of electrically conducting nanorods coated by a layer of pseudocapacitive material. According to preliminary simulations, charge storage on an individual nanorod was not affected by the presence of its neighbors if the distance between adjacent nanorods was larger than 10 nm. Indeed, under this condition, the electric double layers (EDLs) formed near two adjacent coated nanorods did not overlap. Thus, a single axially symmetric nanorod with a conducting nanorod of radius r_i and length L_c conformably coated by a pseudocapacitive layer of thickness L_r was simulated in cylindrical coordinates, as illustrated in Figure 1b. This generic electrode was conceived as a representation of pseudocapacitive electrodes synthesized experimentally.[9–13] Similarly, the electrolyte consisted of $LiClO_4$ in propylene carbonate, as commonly used experimentally.[62]

To make the problem mathematically tractable, the following assumptions were made: (1) the electrolyte was binary and symmetric, i.e., two ion species were considered and featured the same ion diameter a, valency $\pm z$, and diffusion coefficient D. (2) The Stern layer

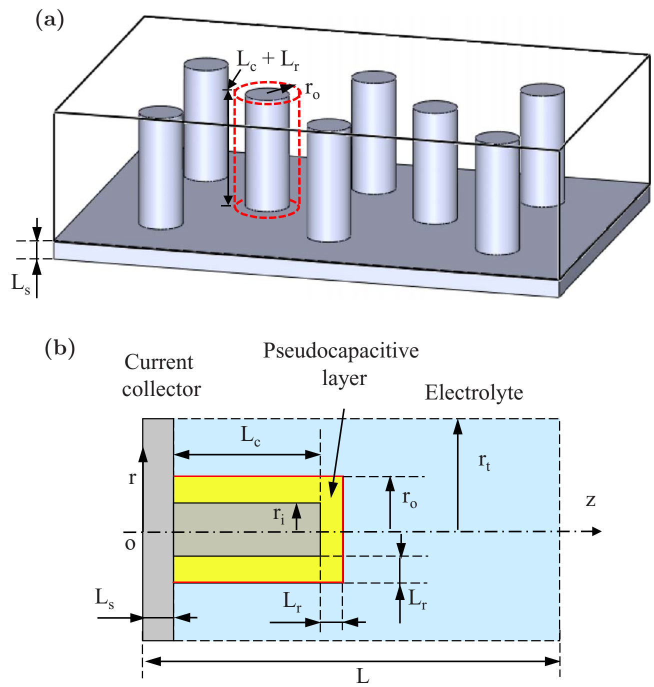

Figure 1. Schematics of (a) electrodes consisting of ordered conducting nanorods coated with pseudocapacitive material on a planar current collector (b) simulated 2D cross-section of one rod along with the cylindrical coordinate system.

contained no free charges and its thickness H was approximated as the radius of the ions, so that $H = a/2$.[52,63,64] (3) The transport properties in the electrode and electrolyte were constant. (4) Bulk motion of the electrolyte was negligible. (5) The system was isothermal and its temperature remained constant.

Governing equations.—The local electric potential $\psi(\mathbf{r}, t)$ in the electrode consisting of a pseudocapacitive layer coated on conducting nanorods was governed by the Poisson equation expressed as[52,65]

$$\nabla \cdot (\sigma_P \nabla \psi) = 0 \quad \text{in the pseudocapacitive layer} \qquad [3]$$

$$\nabla \cdot (\sigma_C \nabla \psi) = 0 \quad \text{in the conducting nanorod} \qquad [4]$$

where σ_P and σ_C are the electrical conductivities of the pseudocapacitive material and of the conducting nanorod, respectively.

The local molar concentration of the intercalated Li^+ (species 1) in the pseudocapacitive layer, denoted by $c_{1,P}(\mathbf{r}, t)$, was governed by the mass diffusion equation given by[65,66]

$$\frac{\partial c_{1,P}}{\partial t} = \nabla \cdot (D_{1,P}\, \nabla c_{1,P}) \qquad [5]$$

where $D_{1,P}$ is the diffusion coefficient of the intercalated Li^+ in the pseudocapacitive layer.

Moreover, the modified Poisson-Nernst-Planck (MPNP) model governed the spatiotemporal evolutions of the electric potential $\psi(\mathbf{r}, t)$ and of the two ion concentrations $c_i(\mathbf{r}, t)$ in the electrolyte.[56,67,68] First, the potential in the electrolyte was governed by the Poisson equation given by[52]

$$\nabla \cdot (\epsilon_0 \epsilon_r \nabla \psi) = \begin{cases} 0 & \text{in the Stern layer,} \\ -zF(c_1 - c_2) & \text{in the diffuse layer.} \end{cases} \qquad [6]$$

Here, $\epsilon_0 = 8.854 \times 10^{-12}$ F m^{-1} is the vacuum permittivity, ϵ_r is the dielectric constant of the electrolyte, z is the valency, and $F = eN_A$ is the Faraday constant. Moreover, the local molar concentrations of cations Li^+ (species 1) and anions ClO_4^- (species 2), denoted by $c_1(\mathbf{r}, t)$ and $c_2(\mathbf{r}, t)$, were governed by the mass conservation equation in the diffuse layer expressed as,[52]

$$\frac{\partial c_i}{\partial t} = -\nabla \cdot \mathbf{N}_i \qquad \text{for } i = 1, 2. \qquad [7]$$

Here, $\mathbf{N}_i(\mathbf{r}, t)$ is the ion mass flux vector of ion species "i" (in mol/m^{2}s) at location $\mathbf{r}$ and time t defined as[52]

$$\mathbf{N}_i(\mathbf{r}, t) = -D\nabla c_i - \frac{zFDc_i}{R_u T}\nabla\psi - \frac{DN_A a^3 c_i}{1 - N_A a^3 (c_1 + c_2)} \nabla(c_1 + c_2) \qquad \text{for } i = 1, 2 \qquad [8]$$

where D and a are the diffusion coefficient and ion diameter of both ion species in the binary and symmetric electrolyte, $R_u = 8.314$ J mol^{-1} K^{-1} is the universal gas constant, and T is the temperature. The three terms on the right-hand side of Equation 8 contributing to the ion mass flux $\mathbf{N}_i$ correspond to ion diffusion, electrostatic migration, and a correction due to finite ion sizes, respectively.[56,69]

Initial and boundary conditions.—In order to solve Equations 3 to 8 for the time-dependent potential $\psi(\mathbf{r}, t)$ and ion concentrations $c_i(\mathbf{r}, t)$ in the conducting scaffold, pseudocapacitive layer, and electrolyte in two-dimensional cylindrical coordinates, one needs one initial condition and two boundary conditions in each direction for each variable in each material.

First, the initial electric potential was assumed to be uniform across the simulated electrode and electrolyte and given by $\psi(\mathbf{r}, 0) = 0$ V. In addition, the initial cation (Li^+) and anion (ClO_4^-) concentrations in the electrolyte were taken as uniform and equal to their bulk concentrations according to $c_1(\mathbf{r}, 0) = c_2(\mathbf{r}, 0) = c_\infty$. Similarly, the initial concentration of intercalated Li^+ in the pseudocapacitive electrode was uniform and equal to $c_{1,P,0}$, i.e., $c_{1,P}(\mathbf{r}, 0) = c_{1,P,0}$.

The potential at the current collector surface $(r, z = 0)$ was imposed as $\psi_s(t)$. For cyclic voltammetry, $\psi_s(t)$ varied linearly with time according to[52]

$$\psi_s(t) = \begin{cases} \psi_{min} + v[t - (n_c - 1)\tau_{CV}] & \text{for } (n_c - 1)\tau_{CV} \le t \le (n_c - 1/2)\tau_{CV} \\ \psi_{max} - v[t - (n_c - 1/2)\tau_{CV}] & \text{for } (n_c - 1/2)\tau_{CV} \le t \le n_c \tau_{CV} \end{cases} \qquad [9]$$

where n_c is the cycle number and τ_{CV} is the cycle period while ψ_{min} and ψ_{max} are the minimum and maximum of the imposed potential, respectively. The corresponding boundary condition in the centerplane located at $\mathbf{r}_{cp} = (0 \le r \le r_t, z = L_s + L)$ was given, by virtue of symmetry, as

$$\psi(\mathbf{r}_{cp}, t) = 0. \qquad [10]$$

The electric potential in the EDL varied linearly across the Stern layer so that the normal electric field at planar and cylindrical Stern/diffuse layer interfaces, located at $\mathbf{r}_H$ satisfied[52,70]

$$\frac{\partial \psi}{\partial n}(\mathbf{r}_H, t) = \frac{\psi(\mathbf{r}_{S/E,pl}) - \psi(\mathbf{r}_H)}{H} \qquad \text{for planar interfaces} \qquad [11]$$

$$-\epsilon_0 \epsilon_r \frac{\partial \psi}{\partial n}(\mathbf{r}_H, t) = C_s^{St}\left(\frac{r_o}{r_o + H}\right)\left[\psi(\mathbf{r}_{S/E,cy}) - \psi(\mathbf{r}_H)\right] \qquad \text{for cylindrical interfaces} \qquad [12]$$

where $\mathbf{r}_{S/E,pl}$ and $\mathbf{r}_{S/E,cy}$ refer to the location of the planar solid/electrolyte interfaces and to that of the cylindrical solid/electrolyte interfaces such that $\mathbf{r}_{S/E,pl} = (r_o \le r \le r_t, z = L_s) \cup (0 \le r \le r_o, z = L_s + L_c + L_r)$ and $\mathbf{r}_{S/E,cy} = (r = r_o, L_s \le z \le L_s + L_c + L_r)$, where r_o is the total radius of the coated nanorod, i.e., $r_o = r_i + L_r$. Here, the Stern layer capacitance C_s^{St} is given by Helmholtz model for cylindrical electrode expressed as[71]

$$C_s^{St} = \frac{\epsilon_0 \epsilon_r}{r_o \ln(1 + H/r_o)}. \qquad [13]$$

These boundary conditions accounted for the presence of the Stern layer without explicitly simulating it in the computational domain. This approach significantly reduced the number of finite elements necessary to numerically solve the equations. In fact, it made possible the numerical solutions of the above coupled transient 2D governing equations.[70]

Moreover, at the current collector/electrolyte interface located at $\mathbf{r}_{C/E} = (r_o \leq r \leq r_t, z = L_s)$, only the capacitive current due to the electric double layer formation contributed to the total current density so that

$$-\sigma_C \frac{\partial \psi}{\partial n}(\mathbf{r}_{C/E}, t) = j_C(\mathbf{r}_H, t) \quad [14]$$

where $\partial/\partial n$ corresponds to the gradient along the direction normal to the electrode/electrolyte interface. Here, $j_C(\mathbf{r}_H, t)$ is the capacitive current density at the Stern/diffuse layer interface located at $\mathbf{r}_H$ and defined as[72]

$$j_C(\mathbf{r}_H, t) = -\epsilon_0 \epsilon_r \frac{\partial^2 \psi}{\partial n \partial t}(\mathbf{r}_H, t). \quad [15]$$

On the other hand, the current density at the pseudocapacitive layer/electrolyte interface, located at $\mathbf{r}_{P/E} = (r = r_o, L_s \leq z \leq L_s + L_c + L_r) \cup (0 \leq r \leq r_o, z = L_s + L_c + L_r)$ equaled to the sum of the capacitive current density $j_C(\mathbf{r}_H, t)$ (in A/m^2) due to EDL formation and the faradaic current density $j_F(t)$ (in A/m^2) due to redox reactions, so that[52,73]

$$-\sigma_P \frac{\partial \psi(\mathbf{r}_{P/E}, t)}{\partial n} = j_C(\mathbf{r}_H, t) + j_F(\mathbf{r}_{P/E}, t). \quad [16]$$

The faradaic current density $j_F(\mathbf{r}_{P/E}, t)$ can be defined by the generalized Frumkin-Butler-Volmer model evaluated at the pseudocapacitive layer/electrolyte interface and expressed as[63]

$$j_F(\mathbf{r}_{P/E}, t) = j_{F,0}(t)\left\{\exp\left[\frac{(1-\alpha)zF\eta(\mathbf{r}_{P/E}, t)}{R_u T}\right] - \exp\left[\frac{-\alpha zF\eta(\mathbf{r}_{P/E}, t)}{R_u T}\right]\right\} \quad [17]$$

where $j_{F,0}(t)$ is the so-called exchange current density, α is the transfer coefficient, and $\eta(\mathbf{r}_{P/E}, t)$ is the surface overpotential. The exchange current density $j_{F,0}(t)$ can be written as[65,73]

$$j_{F,0}(t) = zFk_0[c_1(\mathbf{r}_H, t)]^{1-\alpha}[c_{1,P,max} - c_{1,P}(\mathbf{r}_{P/E}, t)]^{\alpha}[c_{1,P}(\mathbf{r}_{P/E}, t)]^{\alpha} \quad [18]$$

where the reaction rate constant k_0 is expressed in $m^{1+3\alpha}mol^{-\alpha}s^{-1}$ and $c_{1,P,max}$ is the maximum concentration of intercalated Li^+ in the pseudocapacitive layer. In addition, the surface overpotential $\eta(\mathbf{r}_{P/E}, t)$ can be expressed as[63]

$$\eta(\mathbf{r}_{P/E}, t) = \Delta\psi_H(\mathbf{r}_{P/E}, t) - \Delta\psi_{eq}(t) \quad [19]$$

where $\Delta\psi_H(\mathbf{r}_{P/E})$ is the potential drop across the Stern layer at the pseudocapacitive layer/electrolyte interface and $\Delta\psi_{eq}$ is the equilibrium potential difference.

Moreover, the mass flux of the intercalated Li^+ vanished at the conducting nanorod/pseudocapacitive layer interface located at $\mathbf{r}_{N/P} = (0 \leq r \leq r_i, z = L_s + L_c) \cup (r = r_i, L_s \leq z \leq L_s + L_c)$ and at the current collector/pseudocapacitive layer interface located at $\mathbf{r}_{C/P} = (r_i \leq r \leq r_o, z = L_s)$ such that

$$\mathbf{N}_1(\mathbf{r}_{N/P}, t) = \mathbf{N}_1(\mathbf{r}_{C/P}, t) = \mathbf{0}. \quad [20]$$

The mass flux of Li^+ intercalating or deintercalating through the pseudocapacitive layer/electrolyte interface was related to the faradaic current density $j_F(\mathbf{r}_{P/E}, t)$ based on stoichiometry as[74]

$$\mathbf{N}_1(\mathbf{r}_{P/E}, t) = \frac{j_F(\mathbf{r}_{P/E}, t)}{zF}\mathbf{n}_{P/E}. \quad [21]$$

Finally, both the current collector and the pseudocapacitive layer were impermeable to ClO_4^- ions ($i = 2$) so that

$$\mathbf{N}_2(\mathbf{r}_{P/E}, t) = \mathbf{N}_2(\mathbf{r}_{C/E}, t) = \mathbf{0}. \quad [22]$$

Constitutive relationships.—A total of 23 input parameters were needed to solve the governing equations (Equations 3 to 8) along with the initial and boundary conditions. These parameters include (i) the electrolyte properties ϵ_r, a, z, D, and c_∞, (ii) the pseudocapacitive layer properties $\Delta\psi_{eq}$, $c_{1,P,max}$, $c_{1,P,0}$, $D_{1,P}$, k_0, α, and σ_P, (iii) the electrical conductivity of the conducting nanorod and current collector σ_C, (iv) the electrode and electrolyte dimensions r_i, r_t, L, L_c, L_s, and L_r, and (v) the operating conditions T, ψ_{max}, ψ_{min}, and v. Typical values of these parameters were collected from the literature.[47,65,73,75–86]

The binary and symmetric electrolyte simulated corresponded to 1 M $LiClO_4$ in propylene carbonate (PC) solvent, i.e., $c_\infty = 1$ M.[62] The dielectric constant of the electrolyte was taken as constant and equal to $\epsilon_r = 66.1$ corresponding to that of PC at zero electric field.[75] The effective solvated ion diameters a and diffusion coefficient D were taken as those of Li^+ ion ($z = 1$) in PC and equal to $a = 0.67$ nm and $D = 2.6 \times 10^{-10}$ m^2/s.[76]

For electrode consisting of transition metal oxides, the equilibrium potential difference $\Delta\psi_{eq}$ is typically determined experimentally based on open-circuit potentials.[65,73] It can be modeled as a linear function of the state-of-charge (SOC) expressed as $c_{1,P}/c_{1,P,max}$.[47,77,78] For MnO_2 dense films of thickness 100 μm at low scan rates, $\Delta\psi_{eq}(t)$ (in V) was measured as[79]

$$\Delta\psi_{eq}(t) = 10.5[4 - c_{1,P}(t)/c_{1,P,max}] - 39.9. \quad [23]$$

This expression was used in the present study with the maximum intercalated lithium concentration in the pseudocapacitive layer $Li_mM_pO_q$ estimated as $c_{1,P,max} = m\rho/M$ where ρ and M are the density and molar mass of the fully intercalated metal oxide. For $LiMnO_2$, ρ and M were reported as $\rho \approx 3.0$ g/cm^3 and $M = 93.9$ g/mol[80] yielding $c_{1,P,max} \approx 31.9$ mol/L. Finally, the initial concentration of Li^+ in the electrode was chosen as $c_{1,P,0} \approx 6.38$ mol/L such that the initial equilibrium potential difference $\Delta\psi_{eq}(t = 0)$ was zero. In addition, the value of the diffusion coefficient $D_{1,P}$ of the intercalated Li^+ in the transition metal oxides was chosen as 10^{-12} m^2/s, based on the typical range from 10^{-16} to 10^{-10} m^2/s.[81] The reaction rate constant k_0 for transition metal oxides has been reported to range between 10^{-11} and 10^{-8} $m^{2.5}mol^{-0.5}s^{-1}$.[65,73,81] Here, it was taken as $k_0 = 10^{-8}$ $m^{2.5}mol^{-0.5}s^{-1}$ to maximize contribution from redox reactions. The transfer coefficient α was assumed to be 0.5, corresponding to identical energy barriers for forward and backward redox reactions.[63] The electrical conductivity of metal oxides may vary with the intercalation of lithium as well as the structure of the material.[82–84] Here, a constant value $\sigma_P = 10^{-5}$ S/m was selected based on the range of electrical conductivity between 10^{-6} S/m and 10^{-3} S/m for Li_xMnO_2 ($0 \leq x \leq 1$) at room temperature.[83] On the other hand, the electrical conductivity of the conducting nanorod and current collector was taken as the same value of $\sigma_C = 5$ S/m based on the typical range of carbon conductivity between 10^{-6} and 10^2 S/m.[85,86]

Moreover, the thicknesses of the current collector L_s and height of the conducting nanorod L_c were taken as $L_s = 10$ nm and $L_c = 100$ nm. The radius of the conducting nanorod r_i and the thickness of the pseudocapacitive layer L_r were treated as variables. The thickness of the computational domain was taken as $L = 0.5$ μm. The radius of the computational domain r_t was chosen as $r_t = r_i + L_r + 40$ nm.

Finally, the potential window was selected to be large enough to show all relevant phenomena occurring during charging and discharging. Consequently, the imposed potential $\psi_s(t)$ was cycled between $\psi_{min} = -0.2$ and $\psi_{max} = +0.85$ V. The scan rate v varied from 10^{-3} to 10^4 V/s while the temperature was uniform and constant at $T = 298$ K.

Method of solution.—The governing equations along with the initial and boundary conditions were solved using COMSOL 4.4 in parallel computing mode. Mesh element size was chosen to be the smallest at the electrode/electrolyte interface, where the gradients of ion concentrations $c_1(\mathbf{r}, t)$ or $c_2(\mathbf{r}, t)$ and potential $\psi(\mathbf{r}, t)$ were the largest. Numerical convergence was considered to be reached when changes in the local electric potential $\psi(\mathbf{r}, t)$ and the normal component of current density $j_n = \mathbf{j} \cdot \mathbf{n}$ at the electrode/electrolyte interface were less than 1% when reducing the minimum mesh size by a factor of two. In addition, the adaptive time step was controlled by the relative and absolute tolerances set to be both 0.0004. This enabled the use of smaller time steps when potential and current density changed more rapidly with time. The total number of finite elements was on the order of 10^6. The simulations were run on Hoffman2 shared computing cluster of UCLA with 4 to 8 processors and 32 to 64 GB of RAM.

Finally, several cycles were simulated and an oscillatory steady state was considered to be reached when the maximum relative error in $\psi(\mathbf{r}, t)$ and $j_n = \mathbf{j} \cdot \mathbf{n}$ between two consecutive cycles, at time t and t$-\tau_{CV}$, was less than 1%. These conditions were typically met by the third cycle for all conditions simulated. It took around 24 hours CPU time to obtain a numerically converged solution under oscillatory steady-state conditions.

Data processing.—The interfacial area-averaged capacitive current density $j_{C,BET}$, due to EDL formation and dissolution, and faradaic current density $j_{F,BET}$, associated with faradaic reactions, (both in A/m^2) were estimated as

$$j_{k,BET}(t) = \frac{1}{A_{BET}} \iint_{A_{BET}} j_k(\mathbf{r}, t) dA_{BET} \quad \text{with k = C, or F} \quad [24]$$

where A_{BET} is the total surface area of the solid/electrolyte interface, equivalent to that measured experimentally by the Brunauer-Emmett-Teller (BET) method.[87] In addition, the total areal current density was estimated as $j_{T,BET} = j_{C,BET} + j_{F,BET}$.

Moreover, the associated areal integral capacitance $C_{k,BET}$ (in μF/cm^2) can be estimated from the predicted CV curves at scan rate v according to[88]

$$C_{k,BET}(v) = \frac{1}{\psi_{max} - \psi_{min}} \oint \frac{j_{k,BET}(t)}{2v} d\psi_s \quad \text{with} \quad \text{k = C, F, or T.} \quad [25]$$

Similarly, the gravimetric current density $j_{k,g}$ (in A/g) can be expressed as

$$j_{k,g} = j_{k,BET} A_{BET}/m_P \quad \text{with k = C, F, or T} \quad [26]$$

where m_P is the total mass of the pseudocapacitive material coated on the conducting nanorod. Then, the gravimetric capacitance $C_{k,g}(v)$ (in F/g) can be expressed as

$$C_{k,g}(v) = \frac{1}{\psi_{max} - \psi_{min}} \oint \frac{j_{k,g}(t)}{2v} d\psi_s \quad \text{with } k = C, F, \text{ or } T. \quad [27]$$

Results and Discussion

Physical interpretation.—This section considers an electrode consisting of 35 nm thick pseudocapacitive material coated on a conducting nanorod with radius r_i of 5 nm and length L_c of 100 nm (Figure 1b). This configuration was chosen based on experimentally synthesized electrodes consisting of multiple layers of MnO_2 nanocrystals, 10 nm in diameter, deposited on carbon nanotube with outer radius of 7.5 ± 2.5 nm.[11] Figure 2a shows the gravimetric (i) capacitive current density $j_{C,g}$, (ii) faradaic current density $j_{F,g}$, and (iii) total current density $j_{T,g}$ as functions of the imposed potential $\psi_s(t)$ at scan rate $v = 0.1$ V/s. It also shows (b) the corresponding concentrations $c_1(0, L_s+L_c+L_r, t)$ of the cation Li^+ and $c_2(0, L_s+L_c+L_r, t)$ of the anion ClO_4^-, (c) the concentration $c_{1,P}(t)$ of the intercalated Li^+ in the pseudocapacitive layer, and (d) the overpotential η as functions of the imposed potential $\psi_s(t)$. Note that the intercalated Li^+ concentration $c_{1,P}(\mathbf{r}, t)$ was uniform throughout the thin pseudocapacitive layer, i.e., $c_{1,P}(\mathbf{r}, t) = c_{1,P}(t)$.

Figure 2a indicates that the CV curves displayed two regimes namely (i) a faradaic regime in the lower portion of the potential window when contribution by the faradaic current density $j_F(t)$ dominated and (ii) a capacitive regime in the higher portion of the potential window when the capacitive current density $j_C(t)$ dominated. The transition between faradaic and capacitive regimes can be attributed to Li^+ ion starvation in the electrolyte at the pseudocapacitive layer/electrolyte interface during charging, represented by a blue square in Figure 2. Indeed, the exchange current density $j_{F,0}$ (Equation 17) decayed to zero as Li^+ starvation occurred in the electrolyte, i.e., $c_1(\mathbf{r}_H, t) \to 0$. This was caused by faster Li^+ electrodiffusion in the electrolyte away from the electrode/electrolyte interface compared with Li^+ deintercalation from the electrode to the electrode/electrolyte interface due to faradaic reactions. In addition, Figure 2b indicates that ClO_4^- ions formed EDL at the pseudocapacitive layer/electrolyte interface while Li^+ ion concentration reached zero in the capacitive regime. In fact, the ClO_4^- at the pseudocapacitive layer/electrolyte interface reached saturation concentration soon after the onset of the capacitive regime, as indicated by a red circle.

Moreover, Figure 2c indicates that the Li^+ ion concentration $c_{1,P}(t)$ in the pseudocapacitive layer varied linearly with imposed potential in the faradaic regime but remained constant in the capacitive regime. Overall, Li^+ intercalation and deintercalation were fast and reversible despite a small hysteresis at the transition between faradaic and capacitive regimes. Finally, Figure 2d indicates that the overpotential $\eta(t)$ was nearly constant and close to zero in the faradaic regime. However, it was large and varied linearly with time in the capacitive regime, as theoretically explained previously for planar pseudocapacitive electrodes.[39]

Further interpretation of the CV results was obtained by varying the scan rate v between 0.01 and 10^3 V/s. Figure 3a shows the log-log graph of the total gravimetric current density $j_{T,g}$ as a function of scan rate v in log scale for imposed potential $\psi_s(t)$ of 0.1, 0.3, 0.4, and 0.6 V. The slope of $j_{T,g}$ vs. v corresponds to the so-called b-value (Equation 2). Figure 3b shows the b-value for different values of $\psi_s(t)$ during charging. It indicates that the b-value approached unity in both the faradaic and capacitive regimes. However, it featured a dip at the transition from faradaic to capacitive regimes corresponding to the steep drop in the faradaic current density (Figure 2a) due to the ion starvation of Li^+ in the electrolyte at the electrode/electrolyte interface (Figure 2b). Similar observations were made for planar pseudocapacitive electrodes.[55]

Moreover, Figure 3c plots $j_{T,g}/v^{1/2}$ as a function of $v^{1/2}$ for the imposed potential $\psi_s(t)$ of 0.1, 0.3, 0.4, and 0.6 V for scan rate v less than 1 V/s. The slope and intercept corresponded to $k_1(\psi_s)$ and $k_2(\psi_s)$ in Equation 1, respectively. The coefficient of determination R^2 for linear fitting of $j_{T,g}/v^{1/2}$ and $v^{1/2}$ was between 0.96 and 1. To the best of our knowledge, these results provides, for the first time, theoretical validations of the semi-empirical relationship $j_{T,g} = k_1 v + k_2 v^{1/2}$ commonly used experimentally,[29–36] as previously discussed.

Furthermore, Figure 3d shows the gravimetric capacitances (i) $C_{C,g}(v)$ due to the formation of the EDL, (ii) $C_{F,g}(v)$ associated with faradaic reactions, and (iii) $C_{T,g}(v) = C_{F,g}(v) + C_{C,g}(v)$ as functions of scan rate v. It indicates that $C_{C,g}(v)$ was independent of scan rate for $v \leq 10$ V/s and decreased sharply with increasing scan rate for $v \geq 10$ V/s. This was also observed in simulations of planar and porous EDLC electrodes[52] and can be attributed to the fact that the potential propagation across the electrode and/or the ion transport in the electrolyte cannot follow the fast changes in the imposed potential $\psi_s(t)$ at high scan rates. On the other hand, $C_{F,g}$ decreased continuously with increasing scan rate. This was due to the fact that the intrinsically slow faradaic reactions cannot follow the increasingly rapid changes in the imposed potential $\psi_s(t)$. Consequently, the faradaic capacitance $C_{F,g}$ dominated at low scan rates but decreased faster than $C_{C,g}$ with increasing scan rate.

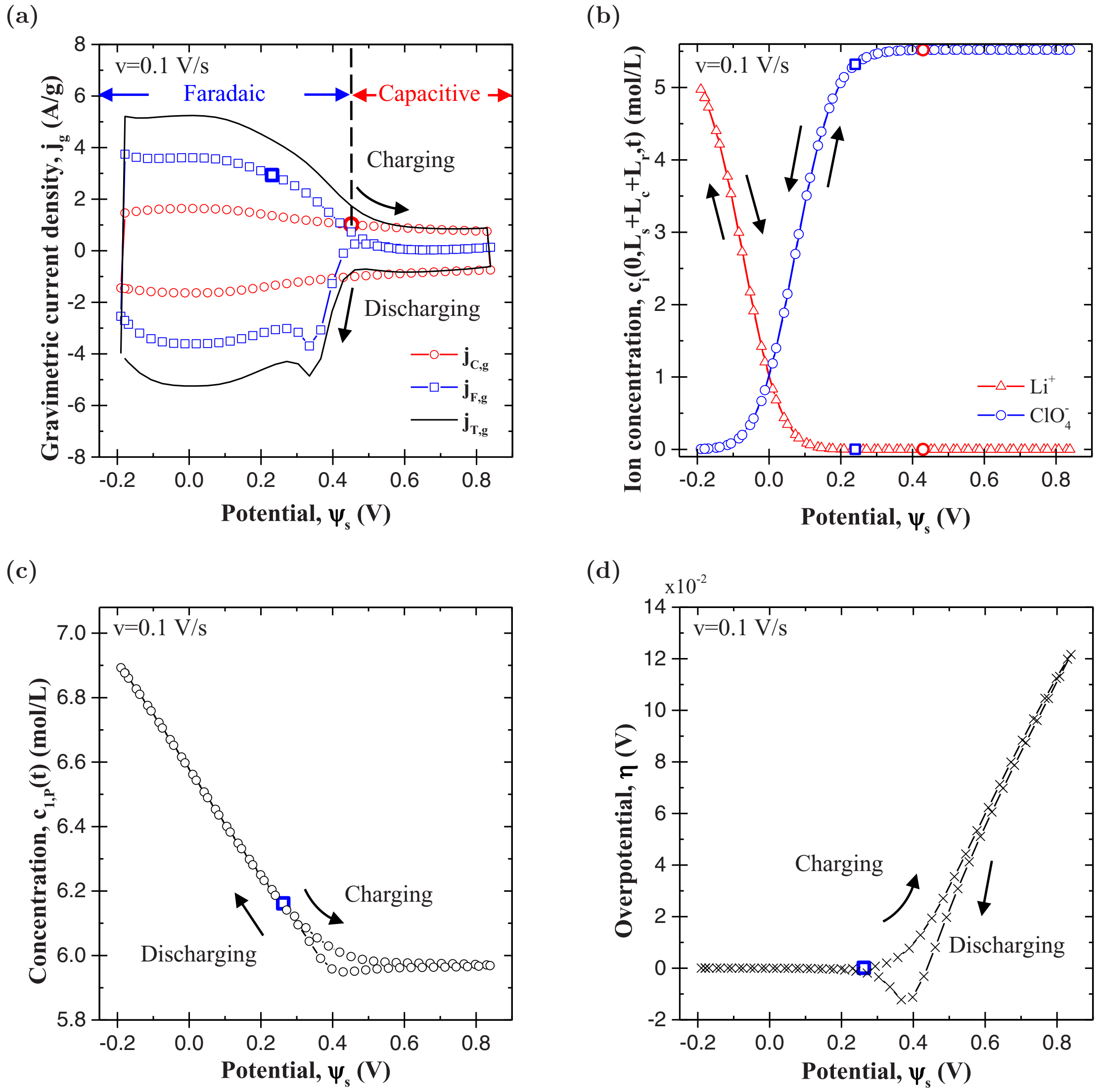

Figure 2. (a) Gravimetric capacitive $j_{C,g}$, faradaic $j_{F,g}$, and total $j_{T,g}$ current densities as functions of imposed potential $\psi_s(t)$ for an electrode consisting of conducting nanorod with radius r_i of 5 nm supporting pseudocapacitive material with thickness L_r of 35 nm, at scan rate $v = 0.1$ V/s. (b) Corresponding Li^+ ion concentration $c_1(0, L_s + L_c + L_r, t)$ and ClO_4^- ion concentration $c_2(0, L_s + L_c + L_r, t)$ at the electrode/electrolyte interface, (c) intercalated Li^+ concentration in the pseudocapacitive layer $c_{1,P}(t)$, and (d) overpotential η as functions of $\psi_s(t)$ at $v = 0.1$ V/s.

Finally, the total capacitance values in Figure 3d at low scan rates (e.g., 65 F/g or 286 F/cm^3 at $v = 0.01$ V/s) were quantitatively comparable with experimentally measured capacitance of 175-250 F/cm^3 for similar electrode structures at the same scan rate.[11] Note that the scan rate in actual CV measurements for pseudocapacitive electrodes ranges typically from 10^{-3} to 1 V/s with no sharp decrease in the total capacitance with increasing scan rate observed.[9,11–13,16] Similar observations could be made in Figure 3d. Here, however, the scan rate v was varied over a wider range to study the rate-dependent capacitance at very high scan rate.

Effect of conducting nanorod radius.—Figure 4 shows (a) the areal capacitive current density $j_{C,BET}$ (in A/m^2) and (b) the gravimetric faradaic current density $j_{F,g}$ (in A/g) as functions of the imposed potential $\psi_s(t)$ for electrodes consisting of conducting nanorod with radius r_i of 5, 35, and 65 nm supporting 35 nm thick pseudocapacitive layer, at scan rate $v = 0.1$ V/s. Figure 4a indicates that the areal capacitive current density $j_{C,BET}$ was independent of r_i. In other words, the total capacitive current i_C (in A) was linearly proportional to the BET surface area A_{BET} such that $i_C \approx j_{C,BET} A_{BET}$, regardless of the radius of the conducting nanorod. Similarly, Figure 4b indicates that the gravimetric faradaic current density $j_{F,g}$ was also independent of r_i and the total faradaic current was linearly proportional to the mass of the pseudocapacitive layer, i.e., $i_F \approx j_{F,g} m_P$. This was attributed to the fast Li^+ intercalation/deintercalation within the volume of the pseudocapacitive layer.

Moreover, Figure 4 shows (c) the areal capacitive capacitance $C_{C,BET}$ and (d) the gravimetric faradaic capacitance $C_{F,g}$ as functions of scan rate v for different values of conducting nanorod radius r_i. These figures indicate that $C_{C,BET}$ was independent of r_i at low scan rates and decreased slightly with decreasing r_i at high scan rates. On the other hand, $C_{F,g}$ was independent of radius r_i at all scan rates considered. Thus, the gravimetric capacitive capacitance $C_{C,g} = C_{C,BET}/(m_P/A_{BET})$ decreased and the areal faradaic capacitance $C_{F,BET} = C_{F,g} m_P/A_{BET}$ increased with increasing mass loading of the pseudocapacitive material m_P/A_{BET} at low scan rates. This explains the fact that the total capacitance $C_T = C_C + C_F$ decreased with increasing m_P/A_{BET} when expressed per BET surface area but increased when expressed per unit mass of the pseudocapacitive layer, as observed experimentally.[10] To further interpret the behaviors of $C_{C,BET}$ and $C_{F,g}$ as functions of scan rate v, one needs to consider the potential propagation across the electrode, the ion

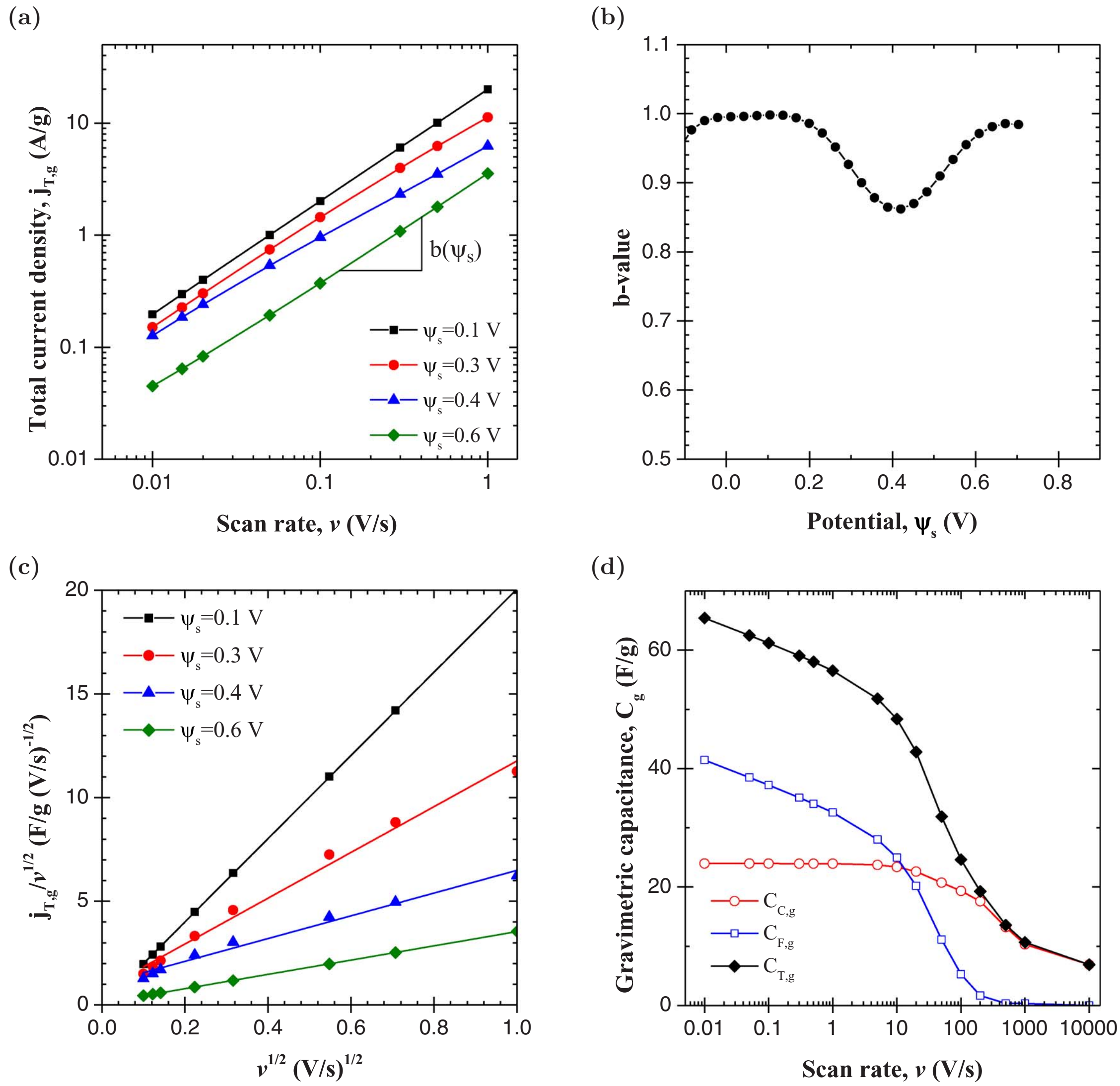

Figure 3. (a) Gravimetric current density $j_{T,g}$ as a function of scan rate v in log-log scale, (b) b-value as a function of the imposed potential $\psi_s(t)$, (c) $j_{T,g}/v^{1/2}$ as a function of $v^{1/2}$ for $v \leq 1$ V/s, and (d) gravimetric capacitive $C_{C,g}$, faradaic $C_{F,g}$, and total $C_{T,g}$ capacitances as functions of scan rate v for an electrode consisting of conducting nanorod with radius r_i of 5 nm supporting pseudocapacitive material with thickness L_r of 35 nm.

transport in the electrolyte at different scan rates, and the Li^+ ion concentration intercalated in the pseudocapacitive layer.

Figures 5a and 5b show the potential $\psi_{tip}(t)$ at the tip of the coated nanorod, located at $(r, z) = (0, L_s + L_c + L_r)$, as a function of the dimensionless time t/τ_{CV} at scan rates $v = 0.1$ and 100 V/s, respectively, for electrodes consisting of conducting nanorod with radius r_i of 5, 35, and 65 nm supporting 35 nm thick pseudocapacitive material layer. At low scan rates, the conducting nanorod radius r_i had no effect on $\psi_{tip}(t)$ which was identical to the imposed potential $\psi_s(t)$ (Figure 5a). However, at high scan rates, a time lag and a reduction in amplitude in $\psi_{tip}(t)$ was increasingly apparent with decreasing nanorod radius (Figure 5b). This was due to the fact that the electrical resistance R_C of the conducting nanorod increased with decreasing r_i according to $R_C = L_c/(\sigma_C \pi r_i^2)$. In addition, Figures 5c and 5d show the corresponding concentrations $c_1(0, L_s+L_c+L_r, t)$ of cations Li^+ and $c_2(0, L_s + L_c + L_r, t)$ of anions ClO_4^- at the electrode/electrolyte interface as functions of the imposed potential $\psi_s(t)$ at scan rates $v = 0.1$ and 100 V/s, respectively. Hysteresis in ion concentrations in the electrolyte were observed only at high scan rates. Moreover, Figures 5e and 5f show the same concentrations $c_1(0, L_s+L_c+L_r, t)$ and $c_2(0, L_s + L_c + L_r, t)$ but as functions of the potential $\psi_{tip}(t)$ at the tip of the coated nanorod, at scan rates $v = 0.1$ and 100 V/s, respectively. It is interesting to note that no hysteresis was observed for $c_1(0, L_s + L_c + L_r, t)$ and $c_2(0, L_s + L_c + L_r, t)$ when plotted versus $\psi_{tip}(t)$ at either scan rates. This indicates that the decrease in $C_{C,BET}$ at high scan rates was due to the slow potential propagation across the electrode. However, it was not due to ion diffusion limitation in the electrolyte. Similar behavior was observed and the same conclusions were reached for 3D simulations of porous EDLC electrodes made of ordered carbon spheres with various values of electrode electrical conductivity and ion diffusion coefficient in the electrolyte.[90] Furthermore, the hysteresis in the concentration $c_{1,P}$ of the Li^+ in the pseudocapacitive layer occurred at all scan rates but was independent of r_i. This led to a continuous decrease in the contribution of faradaic reactions to charge storage and to the decrease of $C_{F,g}$ with increasing scan rate v (Figure 4d).

Effect of pseudocapacitive layer thickness.—Figures 6a and 6b show the areal capacitive current density $j_{C,BET}$ and the gravimetric faradaic current density $j_{F,g}$ as functions of the imposed potential $\psi_s(t)$ for electrodes consisting of conducting nanorod of radius r_i of 5 nm supporting pseudocapacitive layer of thickness L_r of 5, 20, 35, 50, and 100 nm, at scan rate $v = 0.1$ V/s. Figure 6a indicates that the areal capacitive current density $j_{C,BET}$ was independent of L_r. This

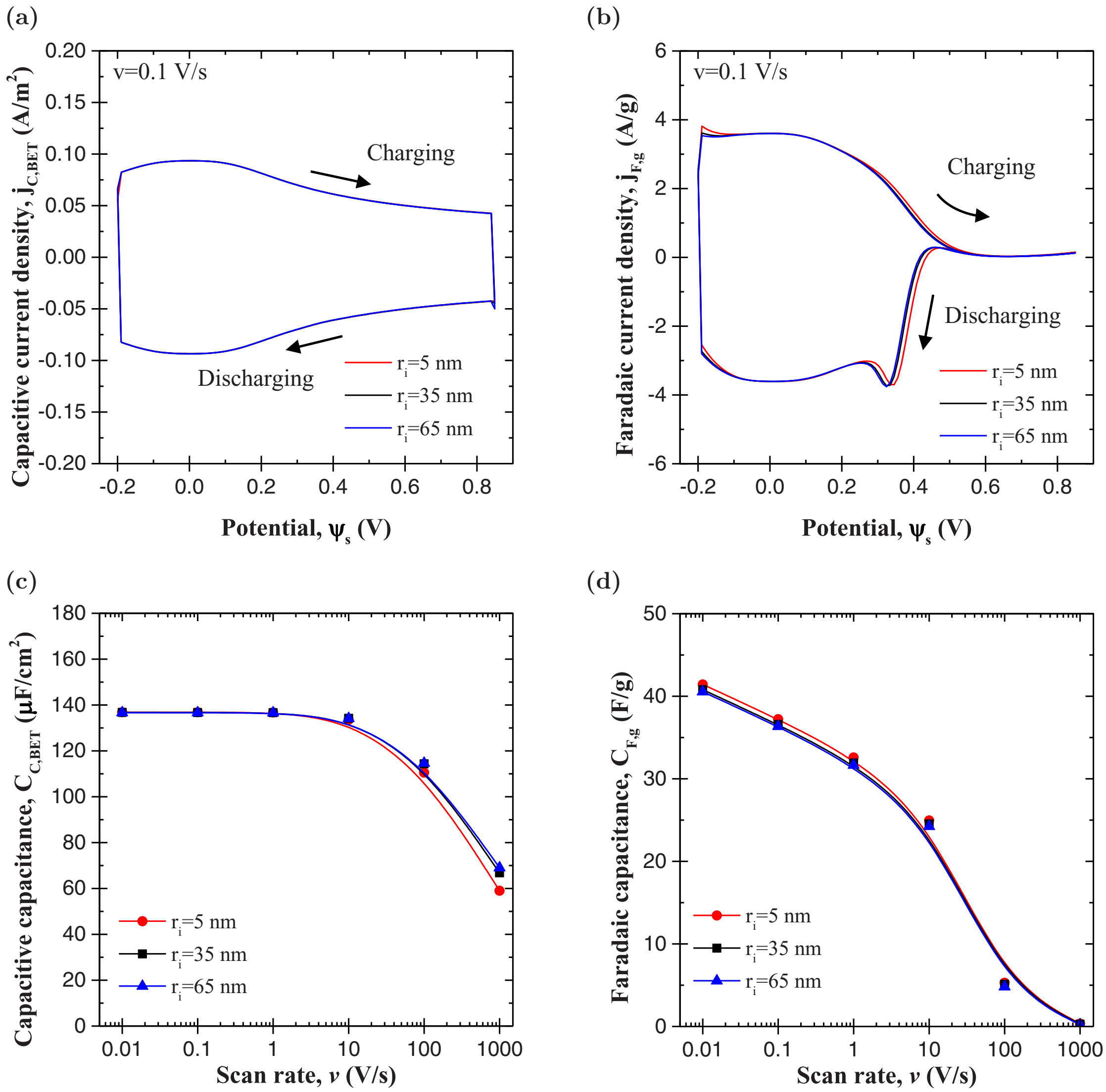

Figure 4. (a)(b) Areal capacitive current density $j_{C,BET}$ and gravimetric faradaic current density $j_{F,g}$ as functions of imposed potential $\psi_s(t)$ at scan rate $v =$ 0.1 V/s, as well as (c)(d) areal capacitive capacitance $C_{C,BET}$ and gravimetric faradaic capacitance $C_{F,g}$ as functions of scan rates v for electrodes consisting of conducting nanorod with radius r_i of 5, 35, and 65 nm supporting pseudocapacitive material with thickness L_r of 35 nm.

was also observed for other conducting nanorod radii r_i. In addition, Figure 6b indicates that the gravimetric faradaic current density $j_{F,g}$ was nearly independent of L_r in the lower portion of the faradaic regime ($\psi_s(t) \leq 0.2$ V). However, for larger potential $\psi_s(t)$, $j_{F,g}$ started decreasing sharply to zero faster with increasing L_r.

To further investigate the effect of L_r, the scan rate v was varied between 10^{-3} V/s and 10^4 V/s. Figure 6c shows the b-value as a function of the imposed potential $\psi_s(t)$ for different values of coating thickness L_r. It indicates that the dip in the b-value became more prominent with increasing pseudocapacitive layer thickness L_r due to a sharper decrease in the total current density $j_{T,g}$ during the transition between the faradaic and capacitive regimes (Figure 6b).

Moreover, Figures 6e and 6f show respectively the areal capacitive capacitance $C_{C,BET}$ and the gravimetric faradaic capacitance $C_{F,g}$ as functions of scan rate v for different values of thickness L_r. It indicates that $C_{C,BET}$ was independent of L_r at low scan rates, corresponding to the equilibrium capacitance, as observed previously for EDLC electrodes.[89] However, it started decreasing sharply and at lower scan rates as L_r increased. In addition, the gravimetric faradaic capacitance $C_{F,g}$ decreased continuously with increasing coating thickness L_r for any given scan rate. Here also, to explain these observations, one needs to consider the temporal evolution of the electrode tip potential, the ion concentrations in the electrolyte at the solid/electrolyte interfaces, as well as the total changes in the state of charge (SOC) during charging.

Figures 7a and 7b show the potential $\psi_{tip}(t)$ at the tip of the electrode, located at $(r, z) = (0, L_s + L_c + L_r)$, as a function of the dimensionless time t/τ_{CV}, for the same electrodes as those simulated in Figure 6, at scan rates $v = 0.1$ and 100 V/s, respectively. Here also, a time lag in the tip potential was observed only at high scan rates associated with a reduction in amplitude in $\psi_{tip}(t)$ which became more apparent with increasing L_r. This was attributed to the increase in electrical resistance $R_P \approx L_r/[\sigma_P(\pi r_i^2 + 2\pi r_i L_c)]$ across the pseudocapacitive layer with increasing L_r at high scan rates. Note that, L_r had a significantly stronger effect on $\psi_{tip}(t)$ than r_i (Figure 5b). This was due to the significantly smaller electrical conductivity of the pseudocapacitive layer σ_P compared with that of the conducting nanorod σ_C. Here also, Figures 7c and 7d show that the corresponding concentrations $c_1(0, L_s + L_c + L_r, t)$ of cations Li^+ and $c_2(0, L_s + L_c + L_r, t)$ of anions ClO_4^- at the electrode/electrolyte interface as functions of the potential $\psi_{tip}(t)$ at the tip of the coated nanorod did not feature any hysteresis, at scan rates $v = 0.1$ and 100 V/s, respectively. Therefore, the decrease in $C_{C,BET}$ at high scan rates, observed in Figure 6e, was only due to slow potential propagation across the electrode and not to ion diffusion limitations in the electrolyte.

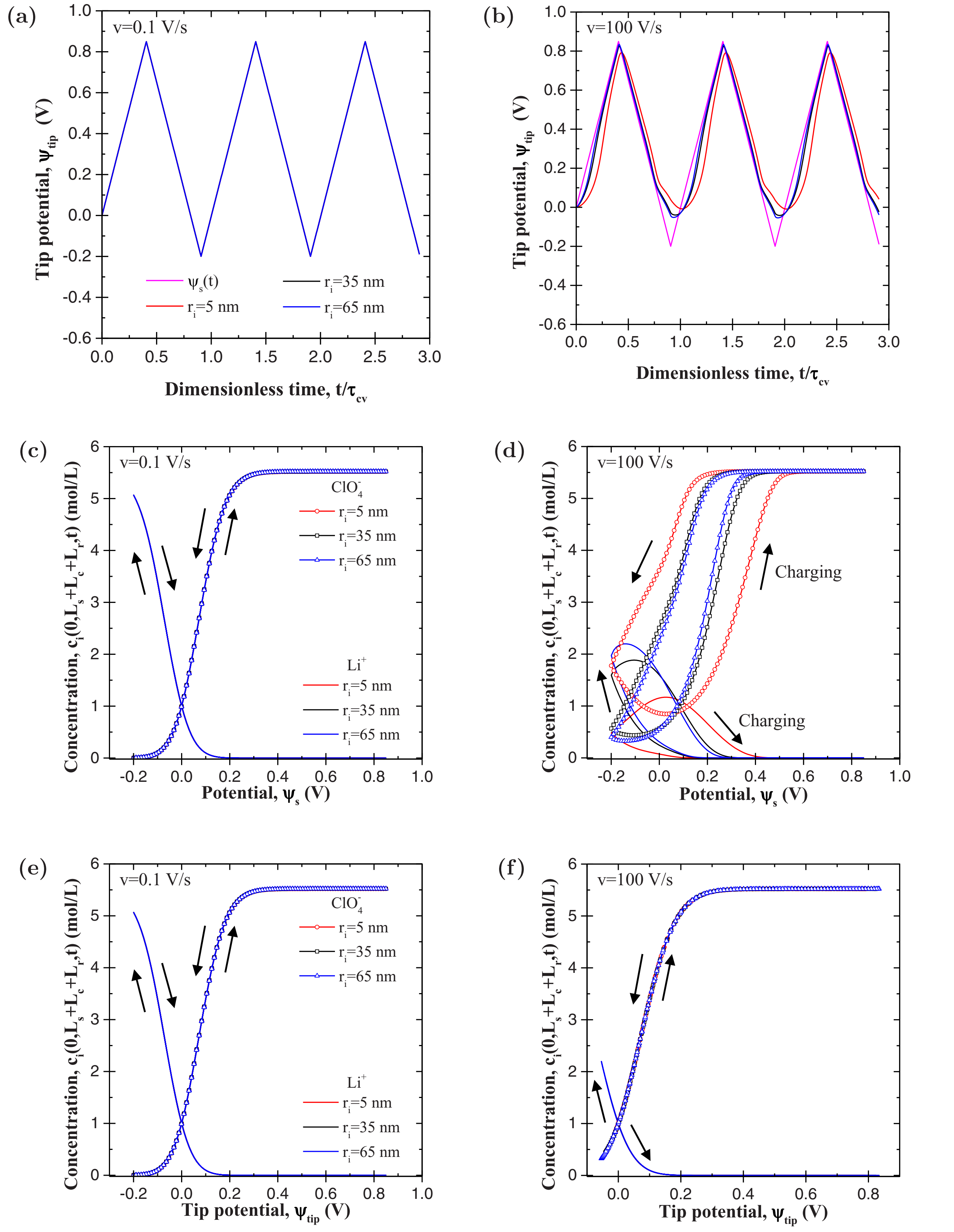

Figure 5. Tip potential $\psi_{tip}(t)$ as a function of the dimensionless time t/τ_{CV}, for electrodes consisting of conducting nanorod with radius r_i of 5, 35, and 65 nm supporting pseudocapacitive material with thickness L_r of 35 nm, at scan rate (a) $v = 0.1$ and (b) 100 V/s. Li^+ ion concentration $c_1(0, L_s + L_c + L_r, t)$ and ClO_4^- ion concentration $c_2(0, L_s + L_c + L_r, t)$ at the electrode/electrolyte interface (c)(d) as functions of the imposed potential ψ_s and (e)(f) as functions of the tip potential $\psi_{tip}(t)$ for the same electrodes at scan rates $v = 0.1$ and 100 V/s.

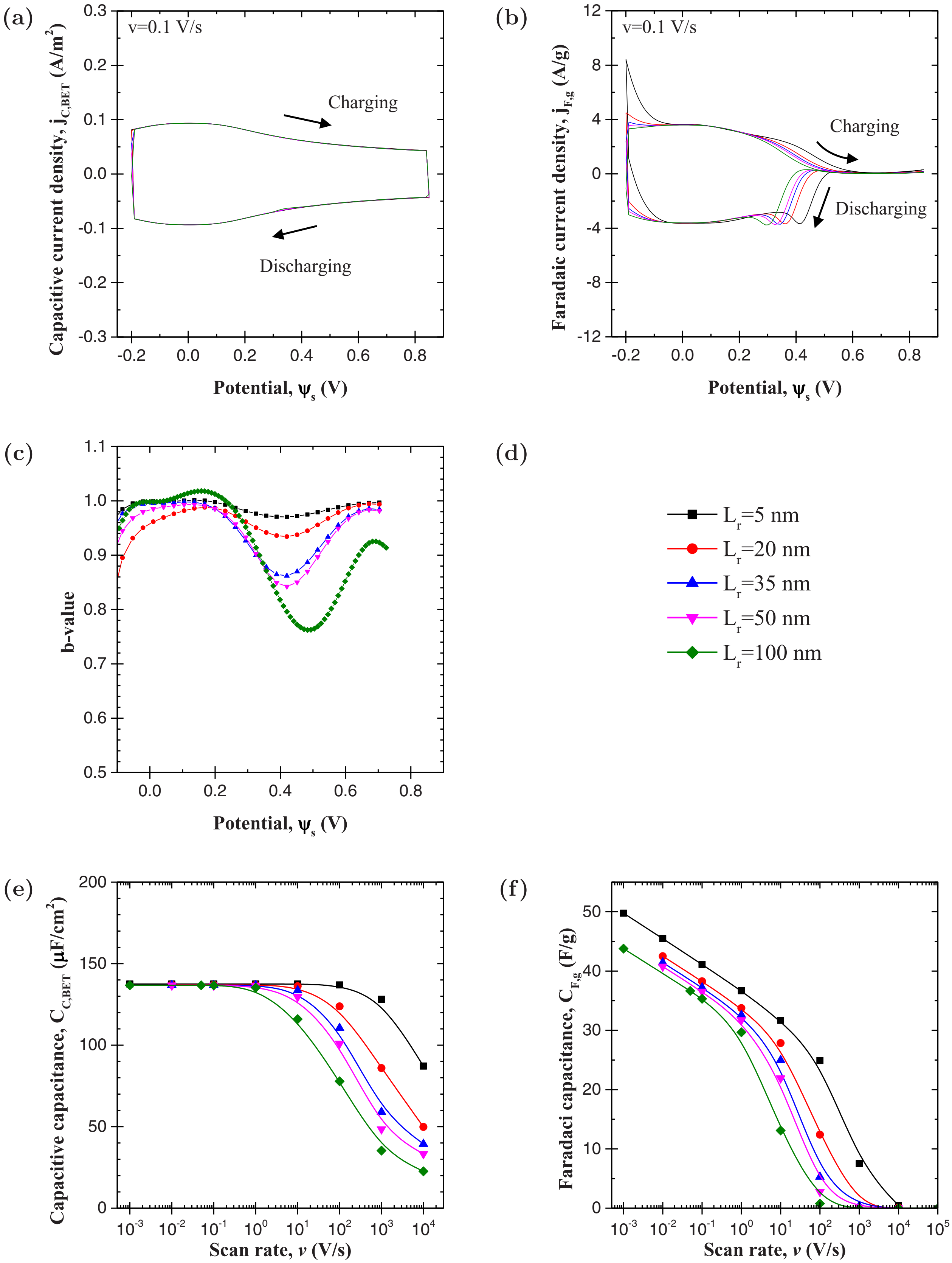

Figure 6. (a)(b) Areal capacitive current density $j_{C,BET}$ and gravimetric faradaic current density $j_{F,g}$ as functions of imposed potential $\psi_s(t)$ at scan rate $v = 0.1$ V/s, (c) b-value as a function of the imposed potential $\psi_s(t)$, and corresponding (e) areal capacitive capacitance $C_{C,BET}$ and (f) gravimetric faradaic capacitance $C_{F,g}$ as functions of scan rates v for electrodes consisting of conducting nanorod with radius r_i of 5 nm supporting pseudocapacitive material with thickness L_r of 5, 20, 35, 50, and 100 nm.

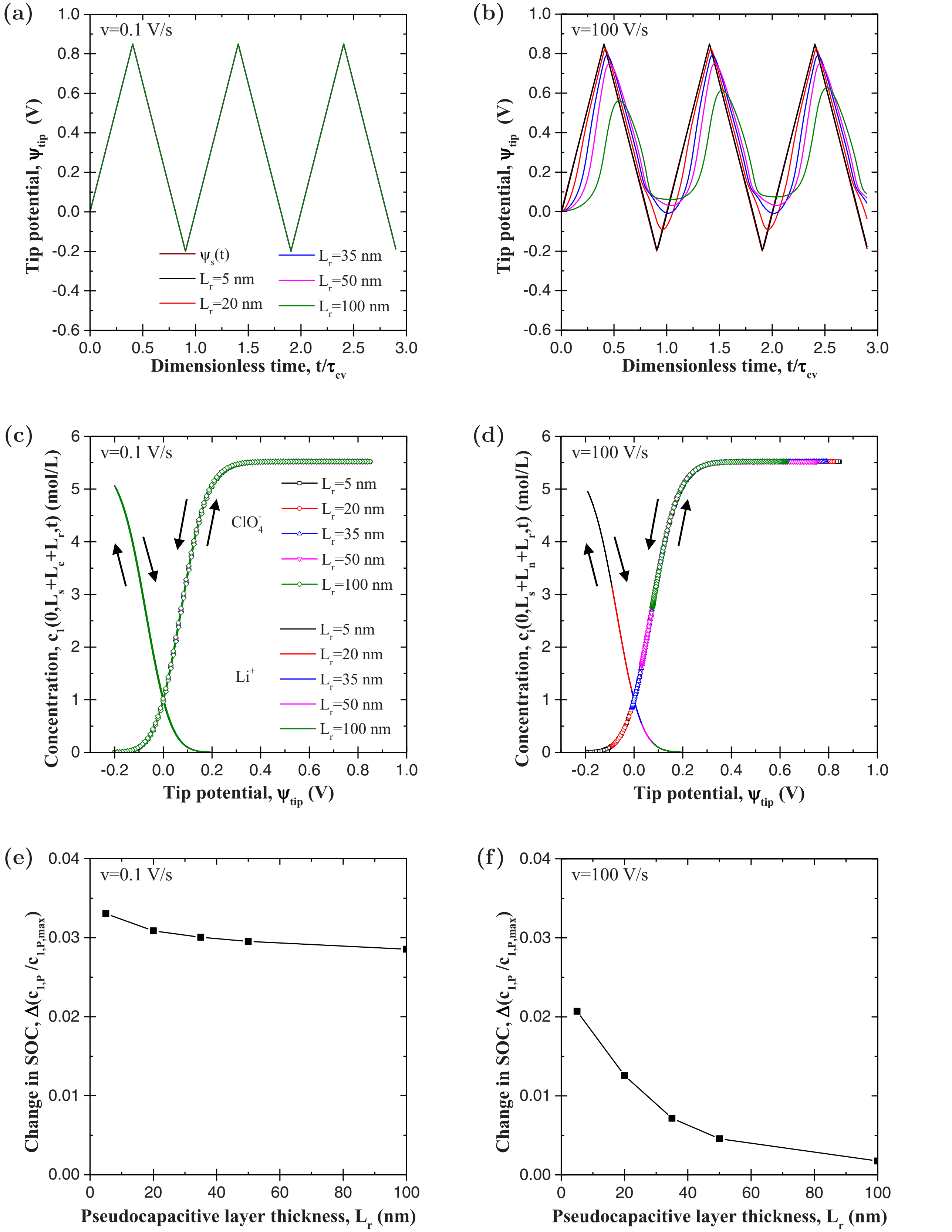

Figure 7. Tip potential $\psi_{tip}(t)$ as a function of dimensionless time t/τ_{CV}, for electrodes consisting of conducting nanorod 5 nm in radius r_i supporting pseudocapacitive material with thickness L_r of 5, 20, 35, 50, and 100 nm, at scan rate (a) $v = 0.1$ and (b) 100 V/s. Corresponding Li^+ ion concentration $c_1(0, L_s + L_c + L_r, t)$ and ClO_4^- ion concentration $c_2(0, L_s + L_c + L_r, t)$ at the electrode/electrolyte interface as functions of the tip potential $\psi_{tip}(t)$ for (c) $v =$ 0.1 and (d) 100 V/s. SOC variation $\Delta(c_{1,P}/c_{1,P,max})$ as a function of the pseudocapacitive layer thickness for (e) $v = 0.1$ and (f) 100 V/s.

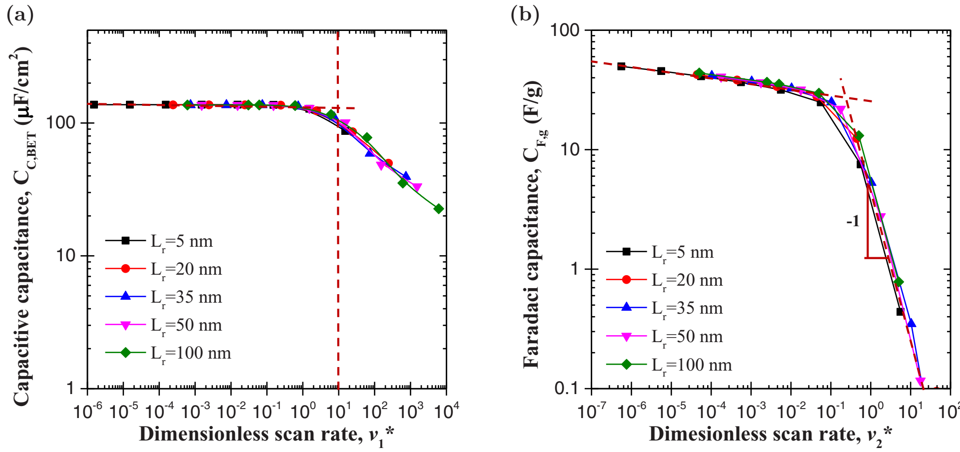

Figure 8. (a) Areal capacitive capacitance $C_{C,BET}$ as a function of dimensionless scan rates v_1^* and (e) gravimetric faradaic capacitance $C_{F,g}$ as a function of dimensionless scan rates v_2^* for electrodes consisting of conducting nanorod with radius r_i of 5 nm supporting pseudocapacitive material with thickness L_r of 5, 20, 35, 50, and 100 nm.

Moreover, Figures 7e and 7f show the total change in SOC, $\Delta c_{1,P}/c_{1,P,max}$, during charging as a function of pseudocapacitive layer thickness L_r, at scan rates $v = 0.1$ and 100 V/s. It indicates that the total change in SOC during charging decreased with increasing scan rate v and thickness L_r. This led to the continuous decrease in charge storage by faradaic reactions and thus to the continuous decrease in $C_{F,g}$ with increasing scan rate v and coating thickness L_r (Figure 6f).

Finally, Figure 8a shows the areal capacitive capacitance $C_{C,BET}$ shown in Figure 6e, for different values of thickness L_r, but as a

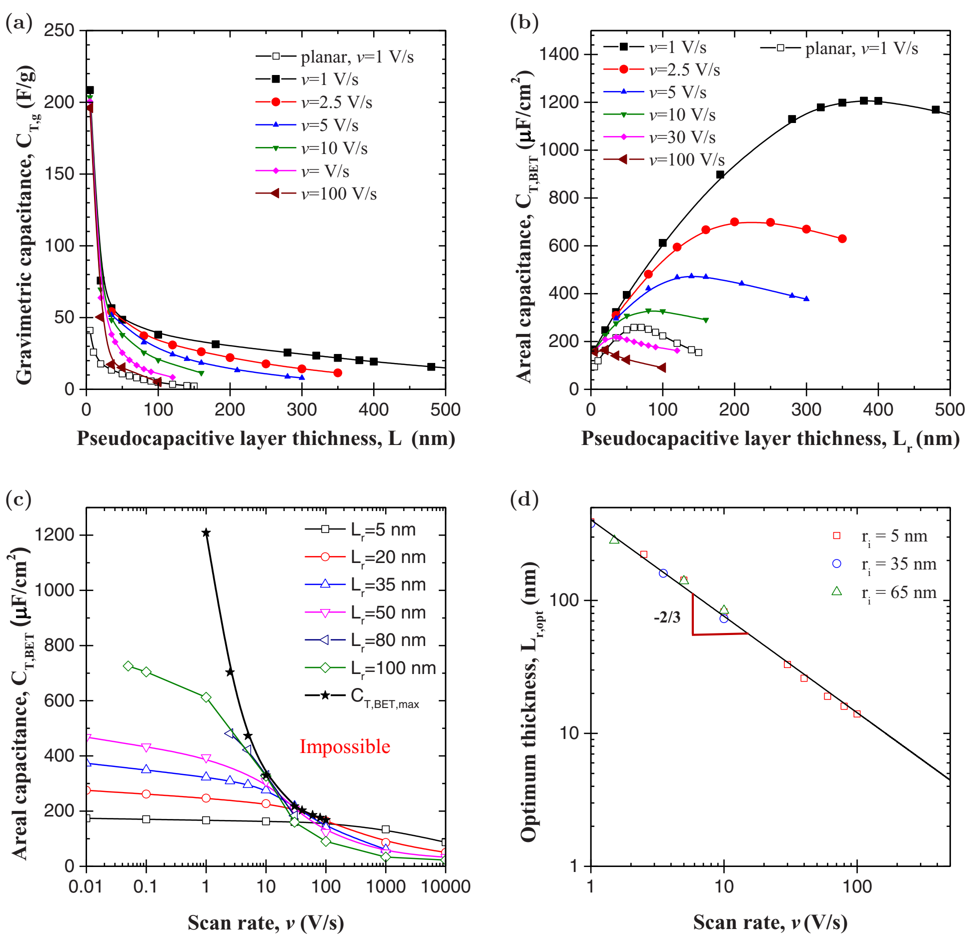

Figure 9. Total (a) gravimetric $C_{T,g}$ and (b) areal $C_{T,BET}$ capacitances as functions of the thickness L_r of pseudocapacitive layer for planar electrodes at scan rate $v = 1$ V/s and for electrodes consisting of conducting nanorod with radius r_i of 5 nm, at scan rates $v = 1$ to 100 V/s. (c) Total $C_{T,BET}$ and maximum possible $C_{T,BET,max}$ areal capacitances as functions of scan rate v for electrodes consisting of conducting nanorod with radius r_i of 5 nm. (d) The optimum thickness $L_{r,opt}$ as a function of the scan rate v for electrodes consisting of conducting nanorod with radius r_i of 5, 35, and 65 nm.

function of dimensionless scan rate v_1^* expressed as[89]

$$v_1^* = \frac{\tau_e}{\tau_{CV}/2} = \frac{v\tau_e}{\psi_{max} - \psi_{min}}. \quad [28]$$

Here, the time scale τ_e was the characteristic time for electron transport across the pseudocapacitive layer expressed as[91]

$$\tau_e = \frac{L_r}{u_e} = \frac{\rho n_e e L_r^2}{M_u(\psi_{max} - \psi_{min})\sigma_P} \quad [29]$$

where u_e is the so-called drift velocity, i.e., the average velocity of electrons under electric field $E = (\psi_{max} - \psi_{min})/L_r$ expressed as $u_e = (M_u\sigma_P E)/(\rho n_e e)$, with n_e the number of free electrons per atom in the pseudocapacitive layer and M_u the atomic mass (in u) of the pseudocapacitive layer. For $LiMnO_2$, $n_e = 1$ and $M_u = 93.9$ u.[92] Figure 8a indicates that the areal capacitive capacitance $C_{C,BET}$, for different values of L_r, collapsed on a single curve and featured self-similar behavior when plotted as a function of dimensionless scan rates v_1^*. Note that Wang and Pilon[89] obtained similar results by scaling τ_{CV} by the ion diffusion time scale in the electrolyte $\tau_D = L^2/D$ instead of τ_e. However, unlike in Ref., 89 the present simulations established that limitations due to potential propagation in the electrode prevailed over ion diffusion limitations in the electrolyte. In addition, the areal capacitive capacitance $C_{C,BET}$ remained constant for $v_1^* \leq 10$.

Similarly, Figure 8b shows the gravimetric faradaic capacitance $C_{F,g}$, shown in Figure 6f, but as a function of dimensionless scan rate v_2^* expressed as[89]

$$v_2^* = \frac{\tau_f}{\tau_{CV}/2} = \frac{v\tau_f}{\psi_{max} - \psi_{min}} \quad [30]$$

where the time scale τ_f associated with faradaic reactions and ion intercalation in the pseudocapacitive layer can be expressed as

$$\tau_f = \sqrt{\tau_i \tau_r}. \quad [31]$$

Here, $\tau_i = L_r^2/D_{1,p}$ is the time scale for ion intercalation in the pseudocapacitive layer treated as a diffusion process.[93] On the other hand, τ_r is the effective time for faradaic reactions that can be expressed as[94]

$$\tau_r = \frac{\sqrt{K}}{k_0(A_{BET}/m)} \approx \frac{\sqrt{K}L_r}{k_0} \quad [32]$$

where K is the equilibrium constant for redox reactions $m\mathrm{Li}^+ + \mathrm{M}_p\mathrm{O}_q + me^- \rightleftharpoons \mathrm{Li}_m\mathrm{M}_p\mathrm{O}_q$ taking place at the pseudocapacitive layer/electrolyte interface. According to chemical thermodynamics, K can be expressed as $K = e^{zFE^0/R_uT}$[95] where E^0 is the standard reduction potential for the above reaction reported relative to standard hydrogen electrode at 1 atm pressure, 298 K temperature, and for 1 M reactant ion (Li^+) concentration in the electrolyte.[96] For Li^+ reacting with MnO_2, $E^0 = -0.16$ V[97] and $K = 1.9 \times 10^{-3}$ at 298 K. Here also, Figure 8b establishes that the capacitance $C_{F,g}$ collapsed on a single curve when plotted as a function of v_2^*. In addition, $C_{F,g}$ was proportional to $(v_2^*)^{-1}$ at high scan rates such that $v_2^* > 0.2$.

Total capacitances and optimum dimensions.—Figure 9 shows (a) the total gravimetric capacitance $C_{T,g}$ and (b) the total areal capacitance $C_{T,BET}$ as functions of pseudocapacitive layer thickness L_r for electrodes consisting of conducting nanorod with radius r_i of 5 nm for scan rate $v = 1$, 2.5, 5, 10, 30, and 100 V/s. Figures 9a and 9b also show $C_{T,g}$ and $C_{T,BET}$ as functions of L_r for a planar electrode with the same electrolyte and electrode properties for scan rate $v = 1$ V/s.[55] The predicted values of the total gravimetric capacitance $C_{T,g}$ ranged between 20 F/g and 200 F/g. These values were comparable with capacitances measured for electrodes with similar morphologies and ranging between 60 F/g and 800 F/g.[9,59,60] Note that the total gravimetric capacitance systematically increased with decreasing pseudocapacitive layer thickness for all scan rates considered. The same trend was also observed for other nanorod radii r_i (not shown). Note that for given electrode and electrolyte dimensions, the total capacitance $C_{T,g}$ or $C_{T,BET}$ for planar pseudocapacitive electrodes increased with increasing electrical conductivity σ_P and ion diffusion coefficient $D_{1,p}$ in the electrode.[55] Moreover, during charging, transport properties $D_{1,p}$ decreased[98] and σ_P increased[99–101] due to the presence of Li^+ intercalated in the metal oxide structure. The dependence of $D_{1,p}$ and σ_P on the local intercalated Li^+ concentration does not seem to be available in the literature and accounting for these processes falls outside the scope of the present simulations. Figure 9b indicates that the total areal capacitance reached a maximum $C_{T,BET,max}$ at an optimum pseudocapacitive layer thickness $L_{r,opt}(v)$, for a given scan rate v. The existence of $L_{r,opt}(v)$ can be attributed to the trade-off between offering large volume of pseudocapacitive layer for volumetric faradaic intercalation of Li^+ while maintaining acceptable potential drop across the electrode. Moreover, Figures 9a and 9b indicate that the total capacitances $C_{T,g}$ and $C_{T,BET}$ as well as the optimum thickness $L_{r,opt}$ for electrodes with conducting nanorod scaffold were much larger than those for planar electrodes[55] for a given scan rate (1 V/s). These observations confirm the positive effect of the conducting scaffold on the electrode performance.

Furthermore, Figure 9c shows the total capacitance $C_{T,BET}$ along with the maximum possible areal capacitance $C_{T,BET,max}$ as functions of scan rate v for pseudocapacitive layer thickness L_r from 5 to 100 nm. The curve for $C_{T,BET,max}$ represents the envelop of the $C_{T,BET}$ - v curves. Any pair (v, $C_{T,BET}$) on the right side of $C_{T,BET,max}(v)$ cannot be reached regardless of thickness L_r.

Finally, Figure 9d shows the optimum pseudocapacitive layer thickness $L_{r,opt}$ as a function of scan rate v for electrodes consisting of conducting nanorod with radius r_i of 5, 35 and 65 nm. It indicates that r_i had a negligible effect on the optimum thickness $L_{r,opt}$ at all scan rates. In addition, the optimum pseudocapacitive layer thickness $L_{r,opt}$ was proportional to $v^{-2/3}$. The power law can be explained by considering the expression of the total capacitance $C_{T,BET}$ as the sum of capacitive and faradaic contributions, i.e., $C_{T,BET}(v, L_r) = C_{C,BET}[v_1^*(L_r)] + C_{F,g}[v_2^*(L_r)]m/A_{BET} \approx C_{C,BET}[v_1^*(L_r)] + C_{F,g}[v_2^*(L_r)]L_r$. In addition, the optimum thickness at any scan rate corresponded to $0.1 \leq v_1^* \leq 10$ and $v_2^* > 1$. Under these conditions, $C_{C,BET}(v_1^*)$ remained constant while $C_{F,g}(v_2^*)$ was proportional to $(v_2^*)^{-1}$, as discussed previously (Figure 8). Therefore,

$$\frac{\partial C_{T,BET}}{\partial L_r} \approx \frac{\partial C_{F,g}}{\partial v_2^*}\frac{\partial v_2^*}{\partial L_r}L_r + C_{F,g} \quad [33]$$

Substituting Equation 30 for $v_2^*(L_r)$ into Equation 33 and solving for the equation $\partial C_{T,BET}/\partial L_r(v, L_{r,opt}) = 0$ yielded $L_{r,opt} = C/v^{2/3}$, where C is a constant depending on the electrode and electrolyte properties as well as the working conditions discussed in Constitutive relationships section.

Conclusions

This paper investigated the effect of nanoarchitecture on the performance of pseudocapacitive electrodes. It presented the first transient multidimensional simulations based on a physicochemical model derived from first-principles for pseudocapacitive electrodes consisting of conducting nanorods coated with a pseudocapacitive layer. First, two semi-empirical approaches commonly used in experiments relating the total current density to the scan rate were numerically reproduced and validated. The simulation tools were also used to determine the respective contributions of EDL formation and faradaic reactions to the total charge storage for different electrode dimensions and scan rates. The areal capacitive capacitance, due to EDL formation, remained constant and independent of electrode dimensions at low scan rates. However, at high scan rates, it decreased more sharply with decreasing conducting nanorod radius and increasing pseudocapacitive layer thickness due to resistive losses. By contrast, the gravimetric faradaic capacitance, arising from reversible faradaic reactions, decreased continuously with increasing scan rate and coating thickness but remained independent of the conducting nanorod radius. Moreover, the predicted total gravimetric capacitance featured realistic values comparable with experimental measurements. Finally, an optimum pseudocapacitive layer thickness to maximize total areal capacitance (in $\mu F/cm^2$) was identified as a function of scan rate and corresponded to a trade-off between achieving large charge storage by using thick pseudocapacitive layer and minimizing resistive losses across the electrode.

Acknowledgments

This research has been supported as part of the Molecularly Engineered Energy Materials, an Energy Frontier Research Center funded by the U.S. Department of Energy, Office of Science, Office of Basic Energy Sciences (Award Number DE-SC0001342). The computation for this study was performed on the Hoffman2 cluster hosted by the Academic Technology Services (ATS) at the University of California, Los Angeles, USA. This material is also based upon work supported, in part, by the China Scholarship Council (CSC).

List of Symbols

a	Effective ion diameter (nm)
a_0, b	Empirical parameters in $j_T = a_0\, v^b$
A_{BET}	Surface area of the electrode/electrolyte interface (m^2)
c_i	Concentration of ion species "i" in the electrolyte (mol/L)
C_{BET}	Areal capacitance (F/m^2)
C_{fp}	Footprint areal capacitance (F/m^2)
C_g	Gravimetric capacitance (F/g)
C_s^{St}	Stern layer capacitance (F/m^2)
$c_{1,P}$	Concentration of intercalated Li^+ in the pseudocapacitive layer (mol/L)
$c_{1,P,0}$	Initial concentration of intercalated Li^+ in the pseudocapacitive layer (mol/L)
$c_{1,P,max}$	Maximum concentration of intercalated Li^+, $c_{1,C,max} = m\,\rho/M$ (mol/L)
D	Diffusion coefficient of ions in electrolyte (m^2/s)
$D_{1,P}$	Diffusion coefficient of intercalated Li^+ in the pseudocapacitive electrode (m^2/s)
e	Elementary charge, $e = 1.602 \times 10^{-19}$ C
E^0	Standard reduction potential for faradaic reactions (V)
F	Faraday constant, $F = eN_A = 9.648 \times 10^4$ C mol^{-1}
H	Stern layer thickness (nm)
i	Magnitude of current (A)
j_{BET}	Magnitude of areal current density (A/m^2)
$j_{F,0}$	Exchange current density due to faradaic reactions (A/m^2)
j_g	Magnitude of gravimetric current density (A/g)
K	Equilibrium constant for faradaic reactions
k_0	Reaction rate constant ($m^{2.5}mol^{-0.5}s^{-1}$)
k_1, k_2	Empirical parameters in $j_T = k_1\, v + k_2\, v^{1/2}$
L	Thickness of the computational domain (nm)
L_c	Length of the conducting nanorod (nm)
L_r	Thickness of the pseudocapacitive layer (nm)
$L_{r,opt}$	Optimum thickness of the pseudocapacitive layer (nm)
L_s	Thickness of the carbon current collector (nm)
m	Stoichiometric number of intercalated Li^+ in $Li_mM_pO_q$
m_P	Mass of the pseudocapacitive layer (g)
M	Molecular weight of the fully intercalated electrode material (g/mol)
M_u	Atomic mass of the pseudocapacitive layer (kg)
$\mathbf{n}$	Vector normal to interfaces
n_c	Cycle number
n_e	Number of free electrons per atom
N_A	Avogadro number, $N_A = 6.022 \times 10^{23}$ mol^{-1}
$\mathbf{N}_i$	Ion flux of species i (mol $m^{-2}s^{-1}$)
p, q	Stoichiometric numbers of the metal and oxygen in the metal oxide M_pO_q
R_C	Electrical resistance of carbon electrode (Ω.
R_P	Electrical resistance across the pseudocapacitive layer (Ω.
r_i	conducting nanorod radius (nm)
r_o	Outer radius of nanorod coated with pseudocapacitive material (nm)
r_t	Radius of region simulated (nm)
$\mathbf{r}$	Location in two-dimensional space (μm)
$\mathbf{r}_{C/E}$	Location of the current collector/electrolyte interface (μm)
$\mathbf{r}_{C/P}$	Location of the current collector/pseudocapacitive layer interface (μm)
$\mathbf{r}_{cp}$	Location of the centerplane (μm)
$\mathbf{r}_H$	Location of the Stern/diffuse layer interface (μm)
$\mathbf{r}_{N/P}$	Location of the nanorod/pseudocapacitive layer interface (μm)
$\mathbf{r}_{P/E}$	Location of the pseudocapacitive layer/electrolyte interface (μm)
$\mathbf{r}_{S/E,cy}$	Location of the cylindrical solid/electrolyte interface (μm)
$\mathbf{r}_{S/E,pl}$	Location of the planar solid/electrolyte interface (μm)
R_u	Universal gas constant, $R_u = 8.314$ J $mol^{-1}K^{-1}$
T	Local temperature (K)
t	Time (s)
u_e	Drift velocity of electrons in the pseudocapacitive layer (m/s)
v	Scan rate of the cyclic voltammetry (V/s)
z	Ion valency

Greek

α	Transfer coefficient, Equations 16 and 17
ϵ_0	Vacuum permittivity, $\epsilon_0 = 8.854 \times 10^{-12}$ F m^{-1}
ϵ_r	Dielectric constant of electrolyte
$\Delta\psi_{eq}$	Equilibrium potential difference (V)
$\Delta\psi_H$	Potential drop across the Stern layer (V)
η	Overpotential, $\eta = \Delta\psi_H - \Delta\psi_{eq}$ (V)
ρ	Density of the fully intercalated pseudocapacitive electrode (kg/m^3)
σ_C	Electrical conductivity of the carbon electrode (S/m)
σ_P	Electrical conductivity of the pseudocapacitive electrode (S/m)
τ_{CV}	Cycle period (s)
τ_D	Time scale for ion diffusion in the electrolyte (s)
τ_e	Time scale for electron transport (s)
τ_f	Time scale for faradaic capacitance (s)
τ_i	Time scale for ion intercalation in the pseudocapacitive layer (s)
τ_r	Effective time for faradaic reactions (s)
ψ	Electric potential (V)
ψ_{min}, ψ_{max}	Minimum and maximum of the potential window (V)
ψ_s	Imposed potential (V)
ψ_{tip}	Potential at the tip of the coated nanorod (V)

Superscripts and Subscripts

∞	Refers to bulk electrolyte
i	Refers to ion species i
F	Refers to faradaic contribution
C	Refers to EDL contribution
T	Refers to total value

References

1. US Department of Energy, "Basic Research Needs for Electrical Energy Storage: Report of the Basic Energy Sciences Workshop for Electrical Energy Storage", Tech. Rep., Office of Basic Energy Sciences, DOE, 2007.
2. P. Simon and Y. Gogotsi, "Materials for electrochemical capacitors," *Nature Materials*, **7**(11), 845 (2008).

3. Y. Zhang, H. Feng, X. Wu, L. Wang, A. Zhang, T. Xia, H. Dong, X. Li, and L. Zhang, "Progress of electrochemical capacitor electrode materials: A review," *International Journal of Hydrogen Energy*, **34**(11), 4889 (2009).
4. G. Wang, L. Zhang, and J. Zhang, "A review of electrode materials for electrochemical supercapacitors," *Chemical Society Reviews*, **41**(2), 797 (2012).
5. Z.-S. Wu, G. Zhou, L.-C. Yin, W. Ren, F. Li, and H.-M. Cheng, "Graphene/metal oxide composite electrode materials for energy storage," *Nano Energy*, **1**(1), 107 (2012).
6. M. S. Halper and J. C. Ellenbogen, "Supercapacitors: A brief overview," Tech. Rep. No. MP 05W0000272, The MITRE Corporation, McLean, VA, 2006.
7. V. Augustyn, P. Simon, and B. Dunn, "Pseudocapacitive oxide materials for high-rate electrochemical energy storage," *Energy & Environmental Science*, **7**(5), 1597 (2014).
8. W. Wei, X. Cui, W. Chen, and D. G. Ivey, "Manganese oxide-based materials as electrochemical supercapacitor electrodes," *Chemical Society Reviews*, **40**(3), 1697 (2011).
9. Q. Li, X.-F. Lu, H. Xu, Y.-X. Tong, and G.-R. Li, "Carbon/MnO_2 double-walled nanotube arrays with fast ion and electron transmission for high-performance supercapacitors," *ACS Applied Materials & Interfaces*, **6**(4), 2726 (2014).
10. Z. Fan, J. Chen, M. Wang, K. Cui, H. Zhou, and Y. Kuang, "Preparation and characterization of manganese oxide/CNT composites as supercapacitive materials," *Diamond and Related Materials*, **15**(9), 1478 (2006).
11. S. W. Lee, J. Kim, S. Chen, P. T. Hammond, and Y. Shao-Horn, "Carbon nanotube/manganese oxide ultrathin film electrodes for electrochemical capacitors," *ACS Nano*, **4**(7), 3889 (2010).
12. C. Y. Lee, H. M. Tsai, H. J. Chuang, S. Y. Li, P. Lin, and T. Y. Tseng, "Characteristics and electrochemical performance of supercapacitors with manganese oxide-carbon nanotube nanocomposite electrodes," *Journal of the Electrochemical Society*, **152**(4), A716 (2005).
13. J. Yan, Z. Fan, T. Wei, W. Qian, M. Zhang, and F. Wei, "Fast and reversible surface redox reaction of graphene–MnO_2 composites as supercapacitor electrodes," *Carbon*, **48**(13), 3825 (2010).
14. A. E. Fischer, K. A. Pettigrew, D. R. Rolison, R. M. Stroud, and J. W. Long, "Incorporation of homogeneous, nanoscale MnO_2 within ultraporous carbon structures via self-limiting electroless deposition: implications for electrochemical capacitors," *Nano Letters*, **7**(2), 281 (2007).
15. H. Zhou, X. Wang, E. Sheridan, H. Gao, J. Du, J. Yang, and D. Chen, "Boosting the energy density of 3D dual-manganese oxides-based Li-ion supercabattery by controlled mass ratio and charge injection," *Journal of The Electrochemical Society*, **163**(13), A2618 (2016).
16. J. W. Lee, A. S. Hall, J.-D. Kim, and T. E. Mallouk, "A facile and template-free hydrothermal synthesis of Mn_3O_4 nanorods on graphene sheets for supercapacitor electrodes with long cycle stability," *Chemistry of Materials*, **24**(6), 1158 (2012).
17. Y. Chen, C. G. Liu, C. Liu, G. Q. Lu, and H. M. Cheng, "Growth of single-crystal α-MnO_2 nanorods on multi-walled carbon nanotubes," *Materials Research Bulletin*, **42**(11), 1935 (2007).
18. G.-X. Wang, B.-L. Zhang, Z.-L. Yu, and M.-Z. Qu, "Manganese oxide/MWNTs composite electrodes for supercapacitors," *Solid State Ionics*, **176**(11), 1169 (2005).
19. V. Subramanian, H. Zhu, and B. Wei, "Synthesis and electrochemical characterizations of amorphous manganese oxide and single walled carbon nanotube composites as supercapacitor electrode materials," *Electrochemistry Communications*, **8**(5), 827 (2006).
20. E. Raymundo-Pinero, V. Khomenko, E. Frackowiak, and F. Beguin, "Performance of manganese oxide/CNTs composites as electrode materials for electrochemical capacitors," *Journal of the Electrochemical Society*, **152**(1), A229 (2005).
21. T. Cottineau, M. Toupin, T. Delahaye, T. Brousse, and D. Belanger, "Nanostructured transition metal oxides for aqueous hybrid electrochemical supercapacitors," *Applied Physics A*, **82**(4), 599 (2006).
22. J. Xiao, L. Wan, S. Yang, F. Xiao, and S. Wang, "Design hierarchical electrodes with highly conductive $NiCo_2S_4$ nanotube arrays grown on carbon fiber paper for high-performance pseudocapacitors," *Nano Letters*, **14**(2), 831 (2014).
23. L. Wan, J. Xiao, F. Xiao, and S. Wang, "Nanostructured (Co, Ni)-based compounds coated on a highly conductive three dimensional hollow carbon nanorod array (HCNA) scaffold for high performance pseudocapacitors," *ACS Applied Materials & Interfaces*, **6**(10), 7735 (2014).
24. Z. Ma, X. Huang, S. Dou, J. Wu, and S. Wang, "One-pot synthesis of Fe_2O_3 nanoparticles on nitrogen-doped graphene as advanced supercapacitor electrode materials," *The Journal of Physical Chemistry C*, **118**(31), 17231 (2014).
25. J. Eskusson, P. Rauwel, J. Nerut, and A. Jänes, "A hybrid capacitor based on Fe_3O_4-graphene nanocomposite/few-layer graphene in different aqueous electrolytes," *Journal of The Electrochemical Society*, **163**(13), A2768 (2016).
26. S. Chen, J. Zhu, X. Wu, Q. Han, and X. Wang, "Graphene oxide- MnO_2 nanocomposites for supercapacitors," *ACS nano*, **4**(5), 2822 (2010).
27. B. Brown, I. A. Cordova, C. B. Parker, B. R. Stoner, and J. T. Glass, "Optimization of active manganese oxide electrodeposits using graphenated carbon nanotube electrodes for supercapacitors," *Chemistry of Materials*, **27**(7), 2430 (2015).
28. A. E. Fischer, M. P. Saunders, K. A. Pettigrew, D. R. Rolison, and J. W. Long, "Electroless deposition of nanoscale MnO_2 on ultraporous carbon nanoarchitectures: correlation of evolving pore-solid structure and electrochemical performance," *Journal of The Electrochemical Society*, **155**(3), A246 (2008).
29. J. Wang, J. Polleux, J. Lim, and B. Dunn, "Pseudocapacitive contributions to electrochemical energy storage in TiO_2 (anatase) nanoparticles," *The Journal of Physical Chemistry C*, **111**(40), 14925 (2007).
30. T. Brezesinski, J. Wang, S. H. Tolbert, and B. Dunn, "Ordered mesoporous α-MoO_3 with iso-oriented nanocrystalline walls for thin-film pseudocapacitors," *Nature Materials*, **9**(2), 146 (2010).
31. Z. Chen, V. Augustyn, X. Jia, Q. Xiao, B. Dunn, and Y. Lu, "High-performance sodium-ion pseudocapacitors based on hierarchically porous nanowire composites," *ACS nano*, **6**(5), 4319 (2012).
32. B. Laskova, M. Zukalova, A. Zukal, M. Bousa, and L. Kavan, "Capacitive contribution to Li-storage in TiO_2 (B) and TiO_2 (anatase)," *Journal of Power Sources*, **246**, 103 (2014).
33. M. C. Lopez, G. F. Ortiz, P. Lavela, R. Alcantara, and J. L. Tirado, "Improved energy storage solution based on hybrid oxide materials," *ACS Sustainable Chemistry & Engineering*, **1**(1), 46 (2012).
34. B. Zhao and Z. Shao, "From paper to paper-like hierarchical anatase TiO_2 film electrode for high-performance lithium-ion batteries," *The Journal of Physical Chemistry C*, **116**(33), 17440 (2012).
35. J.-H. Kim, K. Zhu, J. Y. Kim, and A. J. Frank, "Tailoring oriented TiO_2 nanotube morphology for improved Li storage kinetics," *Electrochimica Acta*, **88** 123 (2013).
36. J. B. Cook, H.-S. Kim, Y. Yan, J. S. Ko, S. Robbennolt, B. Dunn, and S. H. Tolbert, "Mesoporous MoS_2 as a transition metal dichalcogenide exhibiting pseudocapacitive Li and Na-ion charge storage," *Advanced Energy Materials*, **6**(9), (2016).
37. T.-C. Liu, W. Pell, B. Conway, and S. Roberson, "Behavior of molybdenum nitrides as materials for electrochemical capacitors comparison with ruthenium oxide," *Journal of the Electrochemical Society*, **145**(6), 1882 (1998).
38. H. Lindström, S. Södergren, A. Solbrand, H. Rensmo, J. Hjelm, A. Hagfeldt, and S.-E. Lindquist, "Li^+ ion insertion in TiO_2 (anatase). 2. voltammetry on nanoporous films," *The Journal of Physical Chemistry B*, **101**(39), 7717 (1997).
39. H.-L. Girard, H. Wang, A. L. d'Entremont, and L. Pilon, "Physical interpretation of cyclic voltammetry for hybrid pseudocapacitors," *The Journal of Physical Chemistry C*, **119**(21), 11349 (2015).
40. L. Kong, C. Zhang, S. Zhang, J. Wang, R. Cai, C. Lv, W. Qiao, L. Ling, and D. Long, "High-power and high-energy asymmetric supercapacitors based on Li^+-intercalation into a T-Nb_2O_5/graphene pseudocapacitive electrode," *Journal of Materials Chemistry A*, **2**(42), 17962 (2014).
41. J. Li, Z. Tang, and Z. Zhang, "Pseudocapacitive characteristic of lithium ion storage in hydrogen titanate nanotubes," *Chemical Physics Letters*, **418**(4), 506 (2006).
42. E. Lim, H. Kim, C. Jo, J. Chun, K. Ku, S. Kim, H. I. Lee, I.-S. Nam, S. Yoon, K. Kang et al., "Advanced hybrid supercapacitor based on a mesoporous niobium pentoxide/carbon as high-performance anode," *ACS nano*, **8**(9), 8968 (2014).
43. Y.-M. Lin, P. R. Abel, D. W. Flaherty, J. Wu, K. J. Stevenson, A. Heller, and C. B. Mullins, "Morphology dependence of the lithium storage capability and rate performance of amorphous TiO_2 electrodes," *The Journal of Physical Chemistry C*, **115**(5), 2585 (2010).
44. L. Shao, J.-W. Jeon, and J. L. Lutkenhaus, "Porous polyaniline nanofiber/vanadium pentoxide layer-by-layer electrodes for energy storage," *Journal of Materials Chemistry A*, **1**(26), 7648 (2013).
45. C. Lin, J. A. Ritter, B. N. Popov, and R. E. White, "A mathematical model of an electrochemical capacitor with double-layer and faradaic processes," *Journal of the Electrochemical Society*, **146**(9), 3168 (1999).
46. C. Lin, B. N. Popov, and H. J. Ploehn, "Modeling the effects of electrode composition and pore structure on the performance of electrochemical capacitors," *Journal of the Electrochemical Society*, **149**(2), A167 (2002).
47. H. Kim and B. N. Popov, "A mathematical model of oxide, carbon composite electrode for supercapacitors," *Journal of the Electrochemical Society*, **150**(9), 1153 (2003).
48. H. Farsi and F. Gobal, "A mathematical model of nanoparticulate mixed oxide pseudocapacitors; Part I: model description and particle size effects," *Journal of Solid State Electrochemistry*, **13**(3), 433 (2009).
49. H. Farsi and F. Gobal, "A mathematical model of nanoparticulate mixed oxide pseudocapacitors; Part II: the effects of intrinsic factors," *Journal of Solid State Electrochemistry*, **15**(1), 115 (2011).
50. T. Kadyk and M. Eikerling, "Charging mechanism and moving reaction fronts in a supercapacitor with pseudocapacitance," *Journal of The Electrochemical Society*, **161**(3), A239 (2014).
51. L. Pilon, H. Wang, and A. L. d'Entremont, "Recent advances in continuum modeling of interfacial and transport phenomena in electric double layer capacitors," *Journal of the Electrochemical Society*, **162**(5), A5158 (2015).
52. H. Wang, A. Thiele, and L. Pilon, "Simulations of cyclic voltammetry for electric double layers in asymmetric electrolytes: A generalized modified Poisson-Nernst-Planck model," *Journal of Physical Chemistry C*, **117**(36), 18286 (2013).
53. A. L. d'Entremont, H.-L. Girard, H. Wang, and L. Pilon, "Electrochemical transport phenomena in hybrid pseudocapacitors under galvanostatic cycling," *Journal of the Electrochemical Society*, **163**(2), A229 (2016).
54. H.-L. Girard, H. Wang, A. L. d'Entremont, and L. Pilon, "Enhancing faradaic charge storage contribution in hybrid pseudocapacitors," *Electrochimica Acta*, **182**, 639 (2015).
55. H.-L. Girard, B. Dunn, and L. Pilon, "Simulations and interpretation of three-electrode cyclic voltammograms of pseudocapacitive electrodes," *Electrochimica Acta*, **211**, 420 (2016).
56. M. Z. Bazant, M. S. Kilic, B. D. Storey, and A. Ajdari, "Towards an understanding of induced-charge electrokinetics at large applied voltages in concentrated solutions," *Advances in Colloid and Interface Science*, **152**(1-2), 48 (2009).

57. J. A. Staser and J. W. Weidner, "Mathematical modeling of hybrid asymmetric electrochemical capacitors," *Journal of The Electrochemical Society*, **161**(8), E3267 (2014).
58. S. Devan, V. R. Subramanian, and R. E. White, "Transient analysis of a porous electrode," *Journal of The Electrochemical Society*, **152**(5), A947 (2005).
59. Z. Lei, F. Shi, and L. Lu, "Incorporation of MnO_2-coated carbon nanotubes between graphene sheets as supercapacitor electrode," *ACS Applied Materials & Interfaces*, **4**(2), 1058 (2012).
60. P. Yang, Y. Ding, Z. Lin, Z. Chen, Y. Li, P. Qiang, M. Ebrahimi, W. Mai, C. P. Wong, and Z. L. Wang, "Low-cost high-performance solid-state asymmetric supercapacitors based on MnO_2 nanowires and Fe_2O_3 nanotubes," *Nano Letters*, **14**(2), 731 (2014).
61. Z. Ye, B. Wang, G. Liu, Y. Dong, X. Cui, X. Peng, A. Zou, and D. Li, "Micropore-dominant vanadium and iron co-doped MnO_2 hybrid film electrodes for high-performance supercapacitors," *Journal of The Electrochemical Society*, **163**(13), A2725 (2016).
62. S.-B. Ma, K.-W. Nam, W.-S. Yoon, X.-Q. Yang, K.-Y. Ahn, K.-H. Oh, and K.-B. Kim, "A novel concept of hybrid capacitor based on manganese oxide materials," *Electrochemistry Communications*, **9**(12), 2807 (2007).
63. A. J. Bard, L. R. Faulkner, J. Leddy, and C. G. Zoski, *Electrochemical Methods: Fundamentals and Applications*, vol. 2, John Wiley & Sons, Hoboken, NJ, 1980.
64. J. H. Masliyah and S. Bhattacharjee, *Electrokinetic and Colloid Transport Phenomena*, John Wiley & Sons, Hoboken, NJ, 2006.
65. G. M. Goldin, A. M. Colclasure, A. H. Wiedemann, and R. J. Kee, "Three-dimensional particle-resolved models of Li-ion batteries to assist the evaluation of empirical parameters in one-dimensional models," *Electrochimica Acta*, **64**, 118 (2012).
66. C.-W. Wang and A. M. Sastry, "Mesoscale modeling of a Li-ion polymer cell," *Journal of the Electrochemical Society*, **154**(11), A1035 (2007).
67. M. S. Kilic, M. Z. Bazant, and A. Ajdari, "Steric effects in the dynamics of electrolytes at large applied voltages. II. Modified Poisson-Nernst-Planck equations," *Physical Review E*, **75**(2), 021503 (2007).
68. L. H. Olesen, M. Z. Bazant, and H. Bruus, "Strongly nonlinear dynamics of electrolytes in large AC voltages," *Physical Review E*, **82**(1), 011501 (2010).
69. M. S. Kilic, M. Z. Bazant, and A. Ajdari, "Steric effects in the dynamics of electrolytes at large applied voltages. I. Double-layer charging," *Physical Review E*, **75**(2), 021502 (2007).
70. H. Wang and L. Pilon, "Mesoscale modeling of electric double layer capacitors with three-dimensional ordered structures," *Journal of Power Sources*, **221**, 252 (2013).
71. D. Halliday, R. Resnick, and J. Walker, *Fundamentals of Physics*, John Wiley & Sons, Hoboken, NJ, 9th edition, 2010.
72. H. Cohen and J. W. Cooley, "The numerical solution of the time-dependent Nernst-Planck equations," *Biophysical Journal*, **5**(2), 145 (1965).
73. V. R. Subramanian, V. Boovaragavan, V. Ramadesigan, and M. Arabandi, "Mathematical model reformulation for lithium-ion battery simulations: Galvanostatic boundary conditions," *Journal of The Electrochemical Society*, **156**(4), A260 (2009).
74. B. E. Conway, *Electrochemical Supercapacitors: Scientific Fundamentals and Technological Applications*, Kluwer Academic/Plenum Publishers, New York, NY, 1999.
75. G. J. Janz and R. P. T. Tomkins, *Nonaqueous Electrolytes Handbook*, vol. I, Academic Press, New York, NY, 1972.
76. K. Nishikawa, Y. Fukunaka, T. Sakka, Y. Ogata, and J. Selman, "Measurement of $LiClO_4$ diffusion coefficient in propylene carbonate by moiré pattern," *Journal of the Electrochemical Society*, **153**(5), A830 (2006).
77. T. Jow and J. Zheng, "Electrochemical capacitors using hydrous ruthenium oxide and hydrogen inserted ruthenium oxide," *Journal of the Electrochemical Society*, **145**(1), 49 (1998).
78. G. Sikha, R. E. White, and B. N. Popov, "A mathematical model for a lithium-ion battery/electrochemical capacitor hybrid system," *Journal of the Electrochemical Society*, **152**(8), 1682 (2005).
79. P. Guillemet, T. Brousse, O. Crosnier, Y. Dandeville, L. Athouel, and Y. Scudeller, "Modeling pseudocapacitance of manganese dioxide," *Electrochimica Acta*, **67**, 41 (2012).
80. Q. Zhong, B. Huang, J. Ma, and H. Li, "Experimental study on relationship between SOC and OCV of lithium-ion batteries," *International Journal of Smart Grid and Clean Energy*, **3**(2), 149 (2014).
81. A. M. Colclasure and R. J. Kee, "Thermodynamically consistent modeling of elementary electrochemistry in lithium-ion batteries," *Electrochimica Acta*, **55**(28), 8960 (2010).
82. A. Bosman and C. Crevecoeur, "Mechanism of the electrical conduction in Li-doped NiO," *Physical Review*, **144**(2), 763 (1966).
83. J. Molenda, M. Ziemnicki, M. Molenda, M. Bućko, and J. Marzec, "Transport and electrochemical properties of orthorhombic $LiMnO_2$ cathode material for Li-ion batteries," *Materials Science-Poland*, **24**(1), 75 (2006).
84. C. Meneses, M. Macedo, and F. Vicentin, "$Li_xMn_2O_4$ thin films characterization by X-ray, electrical conductivity and XANES," *Microelectronics Journal*, **34**(5), 561 (2003).
85. J. Sánchez-González, F. Stoeckli, and T. A. Centeno, "The role of the electric conductivity of carbons in the electrochemical capacitor performance," *Journal of electroanalytical chemistry*, **657**(1), 176 (2011).
86. L. L. Zhang, R. Zhou, and X. Zhao, "Graphene-based materials as supercapacitor electrodes," *Journal of Materials Chemistry*, **20**(29), 5983 (2010).
87. S. Brunauer, P. H. Emmett, and E. Teller, "Adsorption of gases in multimolecular layers," *Journal of the American Chemical Society*, **60**(2), 309 (1938).
88. H. Wang and L. Pilon, "Reply to comments on "Intrinsic limitations of impedance measurements in determining electric double layer capacitances," by H. Wang and L. Pilon [Electrochimica Acta 63 (2012) 55]," *Electrochimica Acta*, **76**(0), 529 (2012).
89. H. Wang and L. Pilon, "Physical interpretation of cyclic voltammetry for measuring electric double layer capacitances," *Electrochimica Acta*, **64**, 130 (2012).
90. B.-A. Mei and L. Pilon, "Three-dimensional cyclic voltammetry simulations of edlc electrodes made of ordered carbon spheres," 2017 (in press, https://doi.org/10.1016/j.electacta.2017.09.060).
91. D. J. Griffiths, *Introduction to electrodynamics*, Prentice Hall, 1962.
92. A. S. for Metals, *Metals handbook*, vol. 3, The Society, 1967.
93. R. J. Borg and G. J. Dienes, *An introduction to solid state diffusion*, Elsevier, 2012.
94. X. Sanchez-Vila, M. Dentz, and L. D. Donado, "Transport-controlled reaction rates under local non-equilibrium conditions," *Geophysical research letters*, **34**(10), (2007).
95. J. D. Hem, "Chemical equilibria and rates of manganese oxidation," Tech. Rep., USGPO, 1963.
96. W. M. Haynes, *CRC handbook of chemistry and physics*, CRC press, 2014.
97. C. Daniel and J. O. Besenhard, *Handbook of battery materials*, John Wiley & Sons, 2012.
98. A. Van der Ven, G. Ceder, M. Asta, and P. Tepesch, "First-principles theory of ionic diffusion with nondilute carriers," *Physical Review B*, **64**(18), 184307 (2001).
99. J. W. Kim, V. Augustyn, and B. Dunn, "The effect of crystallinity on the rapid pseudocapacitive response of Nb_2O_5," *Advanced Energy Materials*, **2**(1), 141 (2012).
100. B. Orel, M. Maček, J. Grdadolnik, and A. Meden, "In situ UV-Vis and ex situ IR spectroelectrochemical investigations of amorphous and crystalline electrochromic Nb_2O_5 films in charged/discharged states," *Journal of Solid State Electrochemistry*, **2**(4), 221 (1998).
101. M. Maček, B. Orel, and U. O. Krašovec, "The effect of lithiation on the electrochromism of sol-gel derived niobium oxide films," *Journal of the Electrochemical Society*, **144**(9), 3002 (1997).